Impact of buoyant jet entrainment on the thermocline behavior in a single-medium thermal energy storage tank

Wanruo Lou, Nicolas Baudin, Stéphane Roux, Yilin Fan, Lingai Luo

Impact of buoyant jet entrainment on the thermocline behavior in a single-medium thermal energy storage tank

Wanruo LOU[1], Nicolas BAUDIN[1], Stéphane ROUX[1], Yilin FAN[1], Lingai LUO[1,*]

[1]*Nantes Université, CNRS, Laboratoire de thermique et énergie de Nantes, LTeN, UMR 6607, F-44000 Nantes, France*

Abstract

This paper presents the characterization and management of dynamic thermocline behaviors in a single-medium thermocline (SMT) thermal energy storage tank with the aim of its performance improvement. In particular, the flow mixing induced by the entering thermal jet, its impact on the temperature stratification and its mitigation measure are systematically explored by both numerical and experimental methods. Results of CFD simulation and particle image velocimetry (PIV) visualization clearly demonstrate the jet entrainment phenomenon and the typical flow patterns featured by the rising buoyant plumes. For the storage tank with simple inlet port, this thermal jet would cause the thermal overturning, the strong fluid mixing and convection heat transfer, resulting in the degradation of temperature stratification and the thermocline decay ($Ri_{gradient} < 0.25$ at certain positions of the tank). It has also been shown by PIV measurement that the impact of thermal jet, characterized by the jet penetration length, becomes stronger with the increasing injecting flow rate and with the decreasing temperature difference between the injecting and existing fluids.

Orifice baffle-type distributor has then been proposed and optimized, showing clearly its effectiveness for mitigating the impact of thermal jet on the temperature stratification. Both the initial uniform orifice baffle and the optimized orifice baffle distributors are then fabricated and installed into a lab-scale cuboid SMT storage tank. Charging operations are performed under different inlet flow rates (Q_{in}: 0.3 to 1.5 L·min^{-1}) and temperature differences between hot and cold fluids (ΔT: 30 to 50 K). Experimental results obtained show that the optimized distributor could always lead to the better thermal performance (capacity ratio up to 0.94 and charging efficiency up to 0.8) than the initial uniform baffle distributor, providing more flexible operating conditions of the SMT storage systems in different industrial sectors.

Keywords: *Thermal Energy Storage (TES); Single-Medium Thermocline (SMT); Jet entrainment; Flow distributor; Particle Image Velocimetry (PIV); Temperature stratification*

[*] Corresponding author.

E-mail address: lingai.luo@univ-nantes.fr

Nomenclature

Latin letters

Cp	Heat capacity at constant pressure [J·kg^{-1}·K^{-1}]
D	Diameter of TES tank [m]
d	Diameter of inlet/outlet port [m]
d_p	Particle diameter [m]
E	Energy [J]
e	Thickness of the baffles [m]
G_b	Buoyancy-generated turbulent kinetic energy [J·kg^{-1}]
g	Gravitational acceleration [m·s^{-2}]
H	Height of thermocline tank [m]
h_j	Length of jet penetration [m]
$\dot{m}$	Mass flow rate [kg·s^{-1}]
N	Number of orifice [–]
N^2	Squared Brunt-Väisälä frequency [s^{-2}]
Q	Volume flow rate [L·min^{-1}]
q	Heat flux per square meter [W·m^{-2}]
P	Pressure [Pa]
Pe	Péclet number [–]
r	Radius of orifice on the baffle [m]
Re	Reynolds number [–]
Ri	Richardson number [–]
s	Surface area [m^2]
S^2	Squared vertical shear production [s^{-2}]
T	Temperature [K]
T^*	Dimensionless temperature [–]
t	Time [s]
t^*	Dimensionless time [–]
$\bar{t}$	Mean value of all passage times [s]
v	Velocity [m·s^{-1}]
V	Volume [m^3]
V^*	Dimensionless volume [–]
$\bar{v}$	Mean velocity [m·s^{-1}]
W	Side length of the storage tank [m]
x, y, z	Coordinates

Greek symbols

α	Thermal diffusivity [m^2·s^{-1}]
β	Thermal expansion coefficient [K^{-1}]
γ	Adjusting factor [–]
δ	Size of control element [m]

η_{ch}	Charging efficiency [–]
λ	Thermal conductivity [W·m^{-1}·K^{-1}]
μ	Viscosity [kg·m^{-1}·s^{-1}]
ρ	Density [kg·m^{-3}]
σ	Capacity ratio [–]

Subscripts/superscripts

bulk	Bulk
c	Cold temperature
gradient	Gradient
h	Hot temperature
i	Orifice index
in	Inlet
ini	Initial state
j	Optimization step
manifold	Manifold
max	Maximum
$normal$	Normal direction
out	Outlet
p	Seeding particle
$stored$	Stored
$tank$	TES tank

Abbreviations

CFD	Computational Fluid Dynamics
cDAQ	Compact data acquisition system
DMT	Dual-medium thermocline
HTF	Heat transfer fluid
IR	Infrared
LIF	Laser Induced Fluorescence
OBD	Orifice baffle-type distributor
PIV	Particle Image Velocimetry
PTV	Particle Tracking Velocimetry
SMT	Single-medium thermocline
TC	Thermocouple
TES	Thermal energy storage

Introduction

Thermocline-based energy storage system, as one of the advanced thermal energy storage (TES) technologies, has received growing interest in recent years [1,2]. It consists in using only one storage tank containing both hot and cold heat transfer fluids (HTFs) inside but separated from each other by the density difference. The presence of a temperature transition zone in between two fluids is called the thermocline. Compared to the conventional two-tank TES concept, the thermocline system shows the features such as less auxiliary components needed and adjustable energy capacity, highly beneficial for efficient and cost-effective energy conversion and management [3,4].

Single-tank thermocline TES systems can be subdivided into single-medium thermocline (SMT) and dual-medium thermocline (DMT). In SMT system only the HTF itself serves as the heat storage medium whereas in DMT, in addition to the HTF, solid fillers (sensible, latent, or a combination of both) are also used to increase the energy storage capacity and the cost competitiveness [5,6]. Among them, SMT systems have shown the advantages such as the simple implementation, relatively easy operation and high efficiency [7,8], with renewed attention being given to its potential applications in various fields.

During the dynamic charging (or discharging) operations, it is expected that the thermocline zone separating the hot and cold HTFs occupies as small volume of the storage tank as possible: a higher level of thermal stratification leading to the improved storage capacity and energy efficiency of the system. But without the buffering effect of solid fillers inside the tank, the fluid flow behaviors in the SMT storage tank are much more complex, and the calm and stable temperature stratification becomes more difficult to be maintained than in the DMT tank [9]. For a charging operation for example, a certain amount of hot HTF having higher temperature and velocity is suddenly injected into the TES vessel initially occupied by the calm and cold HTF. The entering thermal jet will induce complex and unsteady flow patterns, called the jet entrainment [10,11], as displayed in Fig. 1 and briefly described below.

1) Momentum-dominated regime: the entering jet injected from upper inlet port is governed by the high inertia force.
2) Transition regime: inertia force is dampened by the shear stress and by the buoyancy force due to the local density difference.
3) Buoyancy-dominated regime: eddy advection is driven by the buoyancy force, producing rising fluid streams in the form of plumes. This special flow pattern is also named as buoyant plume in fluid dynamics [12,13]. The rising plumes with higher temperature are gradually cooled down by the surrounding cold fluid in this region.
4) Lateral dispersion regime: the flow goes downwards when the density (temperature) difference disappears compared to the surrounding fluid.

The distance between the injecting inlet to the point where the vertical velocity is equal to zero is defined as the jet penetration length h_j (cf. Fig. 1). Note that the boundary between different flow regimes as well as the value of h_j are not stationary but evolve along with the charging time.

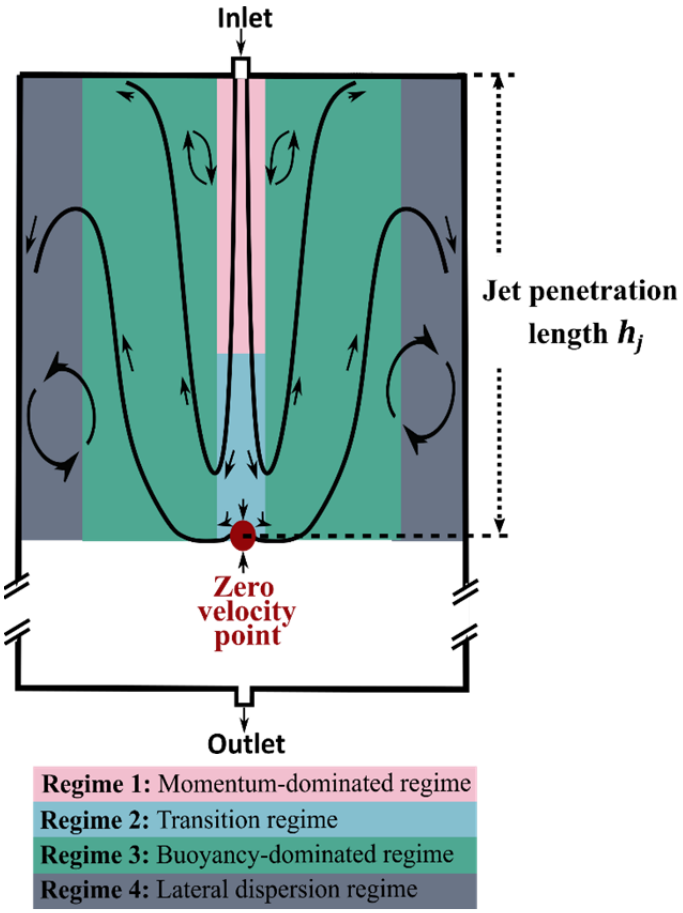

Fig. 1. Schematic of different flow regimes in a SMT storage tank induced by the jet entrainment

The density and velocity differences at the interface of the hot inflowing fluid and the cold surrounding fluid will trigger the Rayleigh-Taylor and Kelvin-Helmholtz instabilities [14], generating the stretched vortex and local turbulences that enhance the fluid mixing [15,16]. Therefore, the time evolution of thermocline could be largely influenced by the jet entrainment phenomenon under certain circumstances. The temperature stratification could also be disturbed, or even damaged by the entering thermal jet and by the resulted buoyant plumes [17,18].

The thermo-hydrodynamic behaviors of the thermal jet and the induced buoyant plumes in confined SMT storage tanks have raised much attention of the researchers [19–21]. These studies distinguish themselves by the presence of analytical, numerical or experimental results, by the use of simple conventional or structured inlet flow distributors, and by the use of different measurement techniques. Nizami et al. [22] developed a novel quasi-1D model for the jet entrainment with above-mentioned four flow regimes, each with their own hydrodynamic features. By including certain correlations like eddy diffusivity in the governing energy equations, their model showed a good agreement with previous experimental results of [23]. Other theoretical models such as the multi-node model [24] and the plume entrainment model [15] have also been proposed, the predicted flow perturbation clearly showing the stratification decay due to the buoyant plumes in the SMT storage tanks. Nevertheless, most theoretical models are based on the simplification of uniform and unidirectional flow [25] while in reality, the velocity distribution at the inlet zone is far more complex due to the sudden expansion and the flow mixing.

Another class of studies are focused on the employment of structured flow diffusing devices to replace the simple inlet/outlet ports so as to mitigate the impacts of the inflowing thermal jet. In this regard, different shapes of flow distributor have been proposed and tested, including tubular distributors (e.g., [26,27]), baffle plates (e.g., [28,29]), radial plates (e.g., [30,31]), hemispherical diffuser [32], porous pipes (e.g., [20,33]), etc. A detailed state-of-the art survey on these flow distributors can be found in [34]. The main purpose is to counterbalance the strong inertia force of the inflowing jet by producing multi-branch streams, inversed flow or radial flow, thereby limiting the impact of thermal jet within a certain depth. Nevertheless, efforts have been focused on the numerical or experimental testing of certain type of diffuser structures while the structure optimization of such distributors are generally lacking.

In terms of experimental measuring techniques, most of the studies installed intrusive temperature sensors within the body of the storage tank to monitor the temperature evolution at several fixed points [35]. However, information on the local velocity profiles, essential for characterizing the jet entrainment phenomenon, cannot be acquired with this method. Very few studies used non-intrusive, optical-based measurement methods like color tracers, Particle Image Velocimetry (PIV) or Laser Induced Fluorescence (LIF) to monitor and analyze the velocity and/or temperature fields of the HTF inside the SMT storage tank. Some of these studies are summarized and listed in Table 1. Berkel et al. [36] used fluorescent dye-based Particle Tracking Velocimetry (PTV) to visualize the thermocline entrainment in a cuboid box and clearly showed the fluid filament, the stretching and folding due to the bucking jet and buoyancy effect. Shah et al. [37] used PIV method to visualize the flow behaviors at the openings of a rigid stratifier and showed that the cold tank water could unexpectedly be sucked into the stratifier. This study has been extended by Andersen et al. [38] by using PIV and LIF measurements for complete flow and temperature fields, with the purpose of validating the numerical model. While the simulated temperature field at certain local positions were in good agreement with the LIF measurements, the spatial and time evolution of entering thermal jet has not been reported. Tinaikar et al. [39] clearly showed plume like structures generated by the vortex pairs at the interface (shadowgraph), and the thermocline thickness increased as a result of the entrainment. Wang and Davidson [40] used PIV measurements to illustrate the fluid dynamic behavior of the three inlet configurations (simple pipe, conic diffuser and porous tube manifold). Their results showed that the manifold structure could largely eliminate the jet mixing and the plume entrainment. Infrared (IR) thermography has also be used to characterize the dynamic temperature evolution in a SMT system [41], but only qualitative analysis was done due to the low-resolution (160×120 pixels) of IR cartography. More recently, the fast camera together with image treatment method has also been used to visualize and monitor the tracer (ink) progression with the injecting flow inside a storage tank [32,42]. The comparison with simple inlet tube showed the interests of structured inlet diffuser on the mitigation of jet entrainment to enhance the stratification. Nevertheless, there is still much room for improvement regarding quantitative and instantaneous experimental measurements.

From the above literature survey, one may find that the real-world experimental investigation on the effects of the jet entrainment and buoyant plumes is still insufficient, especially when it comes to the thermocline evolution inside the SMT storage tank during the charging/discharging operation. Fine modeling and visualization of the complex (transient) flow patterns are mostly needed to identify the

main heat transfer mechanisms resulting in the thermocline decay. Moreover, investigations on the structural optimization of the flow distributors to maintain the temperature stratification are required, as the current available solutions are still far from being sufficient and effective.

This work is aimed to study the impact of buoyant jet entrainment on the thermocline behaviors in the SMT storage tank using a combination of modeling, experimental, analysis and optimization methodologies. The main objectives of this study are threefold: (1) to visualize and characterize the thermo-hydrodynamic behaviors of the injecting flow (jet entrainment) and different flow patterns; (2) to evaluate the impacts of thermal jet on the convective and diffusive heat transfer mechanisms, and on the thermocline evolution inside a SMT storage tank; and (3) to better manage the temperature stratification by optimizing the inlet flow diffuser so as to achieve high energy efficiency of the storage tank. For these purposes, a 3D numerical investigation was firstly performed to optimize the inlet Orifice Baffle-type Distributor (OBD) of the storage tank, using the optimizing algorithm developed in our earlier study [43]. The interactions between the momentum effect and the buoyancy effect on the local velocity and temperature profiles were examined and explained in detail. In particular, the gradient Richardson number and element Péclet number were analyzed and discussed to reveal the effects of convective and diffusive heat transfer on the thermocline decay. Then, the OBDs (initial and optimized) were fabricated and installed into a lab-scale water storage tank. The evolution of the local velocity profiles and flow patterns during the charging operation (hot HTF injecting) were monitored and measured by the PIV method, where the influences of the injecting flow rate and the temperature difference have been particularly addressed. The global performances of the storage tank (characterized by the bulk Richardson number, capacity ratio and charging efficiency) using the initial (uniform) OBD or optimized OBD, were also measured and compared.

Table 1. Selected experimental studies on the optical visualization of thermocline evolution inside the SMT storage tank

Study	Type[a]	Tank geometry	Dimension[b] (m)	Inlet diffuser	T (K)	Re_{in}	Re_{tank}	Numerical model	Experimental Measurement	Remarks
Berkel et al., 2002 [36]	N, E	Cuboid box	0.445 × 0.245 × 0.4	Simple slot	T_h=313-318 T_c=293	475	-	2D and 3D finite difference/volume method without turbulence model	Fluorescent dye colouring based PTV	Visualization of thermocline dynamics and the jet entrainment
Shah et al., 2005 [37]	N, E	Vertical rectangular	*H*=0.9 Cross-section: 0.4 × 0.4	Pipe with lockable openings	T_h=316 T_c=293	-	60	Laminar	PIV/TC	Stratifier worked more efficiently at larger flow rates
Andersen et al., 2008 [38]	N, E	Vertical cylinder	*H*=1.53 *D*=0.7	Pipe with lockable openings or circular openings; fabric stratifier	T_h=323 T_c=293	-	60-300	Realizable *k-ε*	PIV/LIF/TC	Fabric stratifier leaded to the higher temperature gradient than that of other rigid inlet pipes
Tinaikar et al., 2016 [39]	N, E	Glass chamber	0.100 × 0.100 × 0.5	Vortex generator	Ambient temperature	-	-	2D (Ansys CFX)	Shadowgraph	Rising plume induced by partial stripping of the vortex due to buoyancy effect
Wang and Davidson, 2017 [40]	E	Vertical cuboid	*H*=1 Cross-section: 1.02 × 1.02	Simple pipe; pipe with diffuser; porous-tube manifold	T_h=323 T_c=293	1680-7730	97	-	PIV/TC	Porous tube manifold largely eliminated the fluid mixing due to inflowing jet
Gajbhiye et al., 2022 [42]	E	Vertical cylinder	*H*=0.23 *D*=0.11	Porous flow distributor (central or eccentric)	T_h=353-363 T_c=298-303	-	45-179	-	Tracer (ink) progression and image analysis	Influence of the flow distributor, the inlet/outlet positions investigated
Parida et al., 2022 [32]	N, E	Vertical rectangular	0.02 × 0.02 × 0.05	Simple pipe; hemispherical diffuser	Saline and freshwater at ambient temperature	-	-	Finite element Solver, laminar model with conjugate heat transfer	Tracer (ink) progression and image analysis	Compared to simple inlet, the hemispherical diffuser could divert the incoming lighter fluid in an upward direction to achieve better stratification

a. N stands for numerical study and E stands for experimental study

b. *H*: height of the tank; *D*: inner diameter of the tank

2. Methodology

2.1 Experimental setup and procedures

The experimental test-rig shown in Fig. 2 is composed of a thermocline storage tank, hot and cold fluid circuits, a feed tank and the control & data acquisition system. Tap water was used as the HTF in this study. Both hot and cold water tanks (THERMOR Steatis 100L) were equipped with a closed loop driven by a fluid circulator (GRUNDFOS ALPHA120-50N150) to ensure the homogenous fluid condition (e.g., temperature, seeding concentration) at the stand-by state. A built-in heater strip connected to a 1200 W power supply was used as the heat source for the hot water tank and a cryo-thermostat (LAUDA Proline RP 845) was used as the cold source for the cold water tank via an internal helical-coil heat exchanger. The water temperature in each water tank was measured by a PT100 temperature sensor (RS 762-1134). The outflowing fluid from each water tank was filtered by a 20 μm filter (HNP Mikrosysteme F-MI2-T). Two gear pumps (TUTHILL Pump P series, 0.067-7.63 L·min^{-1}) were used to deliver and adjust the flow rate of hot or cold water from the water tank toward the thermocline storage tank (or to the feed tank). The flow rate of each circuit was measured by a calibrated rotating vane flow meter (Kobold DPM 1150 G2, 0.05-5 L·min^{-1} with an accuracy of 1% fs.). The feed tank (300 L) served as a container to store and recycle the HTFs as well as the tracer particles for the PIV measurement.

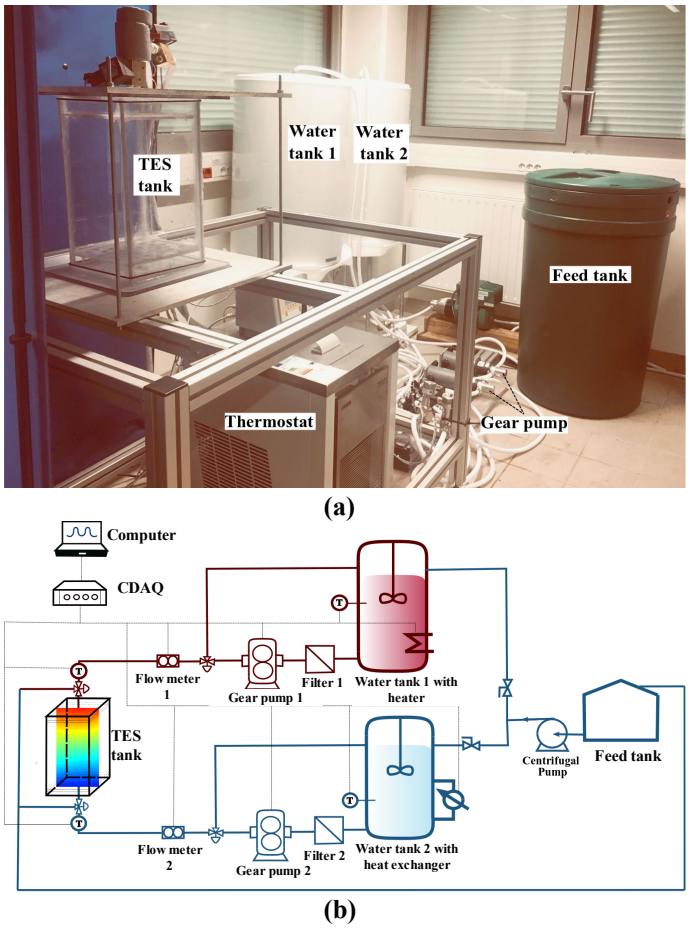

Fig. 2. Test-rig for the lab-scale SMT storage tank. (a) photo view and (b) schematic diagram.

Only the charging operation was investigated, i.e., hot water was injected into the cold water environment to provoke the jet entrainment and the thermocline evolution. Each test was composed of

several steps, following the same protocol described in [29]. The thermocline storage tank was firstly filled up with cold water at temperature T_c. Then hot water at temperature T_h was injected into the tank from the top inlet at a constant flow rate of Q_{in}. The charging operation continued till the tank was fully occupied by the hot water. The inlet and outlet temperatures of water during the whole charging process were measured and recorded by two PT100 (RS 891-9145) sensors additionally calibrated between 0 °C and 80 °C before the experiments. The evolution of fluid velocity profiles inside the storage tank was captured and measured by the PIV facility, described in detail in the following subsection 2.3.

The tightness of the setup was verified before every test to avoid the water leakage. The charging flow rate (Q_{in}) ranged between 0.3 and 1.5 L·min^{-1}, corresponding to an inlet Reynolds number (Re_{in} as defined in Eq. 8) from 1368 to 6831 and an average tank Reynolds number (Re_{tank} as defined in Eq. 9) from 39 to 197. The tested inlet temperature of the hot water T_h ranged from 323.15 to 343.15 K while the cold water T_c was kept at 293.15 K. A LabVIEW platform developed in-house, together with the data acquisition system (NI cDAQ 9178) was used to control the heater strip, the cryo-thermostat, gear pumps and all the electric valves, and to record the measurement data of the flowmeters and the temperature sensors.

2.2 Thermocline storage tank

Figure 3 shows the schematic view of the thermocline storage tank fabricated in the laboratory LTEN. It is a cuboid tank with an inner square cross section of 194 mm of side length (W), and a total inner height (H) of 390 mm. The tank body is made of polycarbonate (ABAQUEPLAST) plates with a thickness of 6 mm, having a good temperature resistance (up to 125 °C) and a good transparency (>90% for visible lights) for PIV measurement. The lateral walls of the tank and the upper & bottom covers were firstly sticking together by a transparent adhesive glue (Araldite Polyurethane 2028) and then sealed by a silicone adhesive glue (Loctite 5366).

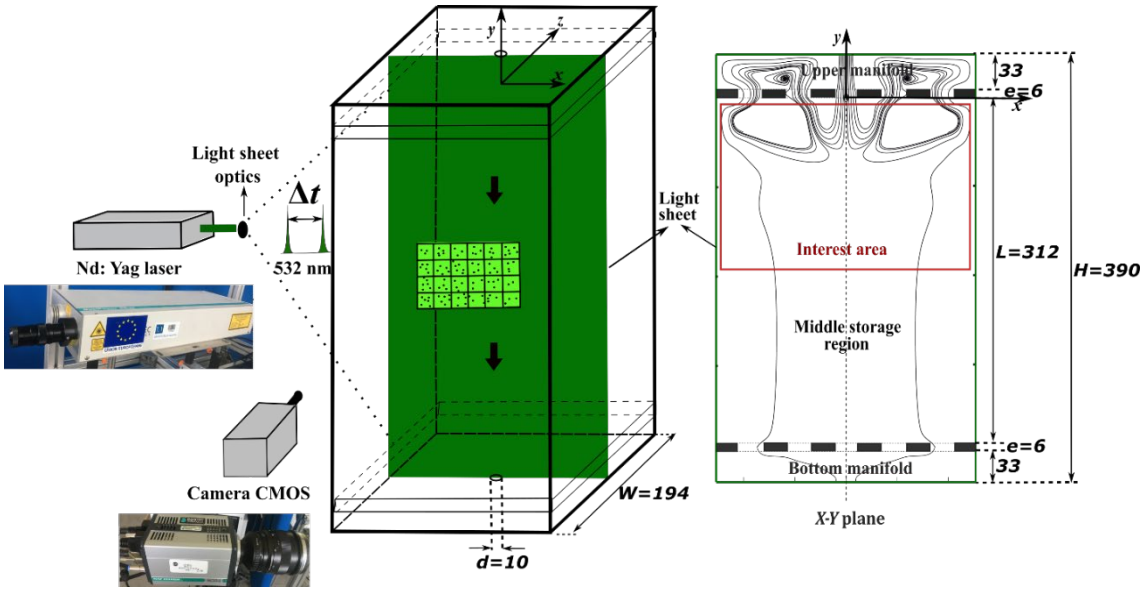

Fig. 3. Schematic view of the cuboid thermocline storage tank, the PIV instruments and the visualization area (unit: mm).

The thermocline storage tank has a single upper and bottom port in the center of the upper and bottom cover, respectively, their inner diameter (*d*) being 10 mm. Two perforated baffles made of polycarbonate were installed into the tank, dividing the inner tank body into three parts (shown in Fig. 3): upper manifold from the upper port to the upper baffle, the middle storage zone and the bottom manifold from the bottom baffle to the bottom port. The height of each part is 33 mm, 312 mm and 33 mm, respectively. The perforated baffles have an overall dimension of 194 mm in length, 194 mm in width and 6 mm in thickness. Each baffle has 37 orifices with uniform or non-uniform diameters subjected to optimization, as will be described in detail in section 3 and Fig. 6. The pipes and valves for entering the hot fluid were insulated by foam glass to reduce the heat loss to the environment.

2.3 PIV setup

PIV technique was used to acquire the instantaneous HTF velocity fields during the charging operations. Polyamid seeding particles (DANTEC PSP-5) with an average diameter of 5 μm and a density of 1030 kg·m^{-3} were used as the seeding in our study. The proportion of seeding was adjusted to be more than 7.5 g·m^{-3} during the experiments. The particle response time can be estimated as $\frac{\rho_p d_p^2}{18\,\mu} \approx 1\,\mu s$ while the flow response time can be estimated as $\frac{d_p}{v_{max}} \approx 25\,\mu s$. The Stokes number defined as the particle response time over the flow response time was always smaller than 0.05 ($\ll 1$) in our condition, indicating that such seeding particles follow the flow streamlines well. The PIV facility consists of illumination unit, image record unit, synchronous controlling unit and data processing unit. The light source used was a double cavity Nd-Yag laser (Litron Nano S65-15PIV serial LM1138). The maximum pulsed energy was 65 mJ with the minimum pulse duration at 4 ns and the wavelength of 532 nm. A cylindrical lens was used to spread the laser beam in a light sheet of about 1.5 mm in thickness, crossing perpendicularly through the walls of the tank along the center line (*z*=0) as shown in Fig. 3. The adaptive settings were employed, e.g., 4 Hz pulse frequency and 2 ms time interval between two frames for the charging flow rate Q_{in} =1 L·min^{-1} with the initial uniform OBD. The number of images during the observation duration (750 s) was kept at 3000 for each measurement. Considering the velocity convergence of PIV measurement, the mean velocity of different number of images from 1 to 2000 has been verified. The velocity perturbations could be largely eliminated when the number of averaging images was higher than 20 (5 s). The choice of averaging images number is a compromise between the quality of images to well represent an instantaneous velocity map, while capturing the long-term development of the flow inside the tank which is intrinsically unsteady.

The light scattered from the small particles was collected by a camera (DANTEC Zyla 5.5) with a 2560 × 2160 pixels CMOS sensor equipped with a 105 mm optic lens. The visualization window was located at the downstream of the upper baffle so as to study the effect of flow distributor on the flow field and its time evolution. The interest area was therefore a *x*-*y* plane (*z*=0) as displayed in Fig. 3. A synchronizer was used to guarantee that the laser and the camera work synchronously.

The commercial software Dynamic studio (release 6.9) was used to control the PIV facility. The data acquisition and image analysis involved three steps:

1) *Image pre-processing:* background image subtraction via minimum value according to the time series;

2) *Correlation calculation:* adaptive correlation performed (initial pass: 64×64 pixels, final pass doubled: 16×16 pixels with a 50% overlap after several attempts considering a compromise between the measurement accuracy and the computational time).
3) *Spurious vector detection:* validation steps (median filter, etc.) to eliminate erroneous velocity vectors.

The spatial resolution was set as 190 mm/ 2360 pixels for the initial uniform OBD case and the final number of velocity vectors in the visualization window was 17080 (=140×122); As for the optimized OBD, the spatial resolution was set as 110 mm/2200 pixels and the final number of velocity vectors was 12500 (=125×100).

2.4 Numerical parameters

3D computational fluid dynamics (CFD) simulations were performed to calculate the transient velocity & temperature characteristics inside the storage tank, providing information for the orifice size optimization of the upper baffle. The following assumptions and simplifications have been made for this study.

- Incompressible Newtonian fluid;
- Temperature-dependent thermophysical properties of fluid, as listed in Table 2;
- An eighth of 3D domain simulated due to its symmetrical geometry (cf. Fig. 6);
- Negligible heat loss to the environment;
- Constant injecting HTF temperature (T_{in}) and flow-rate (Q_{in}) for charging;
- Homogeneous temperature profile T_c=293.15 K in the storage tank at the initial state (t_0), including solid (baffles) and liquid domains.

Table.2. Thermo-physical properties of the fluid and solid (293.15 K<T<333.15 K) [29]

Material	Property	Unit	Fitting correlation *T* (K)
Water	Density *ρ*	kg·m^{-3}	$739.57 + 1.9908T - 0.0038\,T^2$
	Specific heat *Cp*	J·kg^{-1}·K^{-1}	$5438.6 - 8.07T + 0.0129T^2$
	Thermal conductivity *λ*	W·m^{-1}·K^{-1}	$-0.7888 + 0.0077T - 1 \times 10^{-5}\,T^2$
	Viscosity *μ*	kg·m^{-1}·s^{-1}	$0.0215 - 1.198 \times 10^{-4}\,T + 1.701 \times 10^{-7}\,T^2$
Polycarbonate	Density *ρ*	kg·m^{-3}	1200
	Specific heat *Cp*	J·kg^{-1}·K^{-1}	1200
	Thermal conductivity *λ*	W·m^{-1}·K^{-1}	0.2

The following initial and boundary conditions were applied:

(i) Initial conditions were zero velocities and uniform temperature.

$$v_x = 0;\ v_y = 0;\ v_z = 0; T = T_c \tag{1}$$

(ii) At inlet, hot HTF (T_h=333.15 K) was injected into the upper port:

$$v_y|_{y=in} = v_{in} = 0.2122\ \text{m·s}^{-1}\ (\text{for}\ Q_{in} = 1\ \text{L·min}^{-1}) \tag{2}$$

$$T_y|_{y=in} = T_h \tag{3}$$

(iii) Zero static pressure outlet at the bottom port:

$$P_{out} = 0 \tag{4}$$

(iv) At symmetry planes (zero normal velocity and zero normal gradients of all variables):

$$v_{normal} = 0 \tag{5}$$

(v) Conduction heat transfer in the solid domain (OBDs):

$$q = \lambda_s \frac{\partial T}{\partial x} \text{ (e.g., in } x\text{-direction)} \quad (6)$$

Where λ_s is thermal conductivity of polycarbonate.

(vi) Adiabatic top, bottom and lateral walls of TES tank:

$$\frac{\partial T}{\partial y}|_{y=-H,0} = 0;\ v_x = 0;\ v_y = 0;\ v_z = 0 \quad (7)$$

Fluid flow and heat transfer characteristics in the storage tank were calculated using ANSYS FLUENT code (version 19.1). The operational pressure was fixed at 101 325 Pa. Finite-volume method with collocated grid at vertex was applied for numerical discretization. Second-order upwind differential scheme was applied for momentum and standard method for pressure. SIMPLE method was used for the pressure–velocity coupling in order to correct the pressure field oscillations.

Turbulent effect should be considered in the simulation due to the strong jet mixing of fluids with different velocities and densities. Therefore, most of the earlier experimentally validated numerical studies (e.g., [15,27,44]) tended to use a turbulence model rather than the laminar model, despite the low Re_{tank} value (usually smaller than 200). The choice of turbulence model depends on the type of fluid, the working conditions, the required level of accuracy, the available computational resources and the needed time. In this study, the realizable k–ε two-equation model was used. Standard wall functions were used for the near-wall region [45,46]. This model can take the buoyancy effect into account by enabling the full buoyancy option, the generation of turbulence kinetic energy due to the buoyancy G_b being considered for both the transport equations of k and ε.

Simulations were performed under transient state with fixed time step of 0.001 s. Hexahedral elements, multi-zone method, sweep method were applied for meshing fluid and solid domains. A grid independence study was conducted with the increased number of total elements from 1.0 million to 1.4 million. It was found that the deviation of the mean passage time $\bar{t}$ (cf. Eq. 21) at 1.0, 1.1 and 1.4 million mesh was smaller than 0.01%. The grid with 1.1 million elements has finally been chosen for this study. The solution was considered to be converged when (i) normalized residuals were smaller than 8×10^{-5} for mass, momentum, *k* and *ε* equations and 10^{-7} for the energy equation, and (ii) the inlet static pressure become constant (less than 0.5% variation). Simulations were carried out by a computer with 2.2 GHz Intel processors (Intel Xeon CPU E5-2630 v4) and 32.0 GB RAM. The average calculation time of 18 days was required for one fully charging operation.

2.5 Characteristic indicators and dimensionless numbers

The Reynolds number at the inlet port and at the tank body can be calculated by Eqs. 8 and 9, respectively.

$$Re_{in} = \frac{\rho v_{in} d}{\mu} \quad (8)$$

$$Re_{tank} = \frac{\rho \bar{v}_{tank} W}{\mu} \quad (9)$$

Where $\bar{v}_{tank}$ is the mean velocity at the tank body. The physical properties of the HTF used for the calculation were based on the inlet temperature of the fluid (T_h).

The element Péclet number (Pe) is introduced here to characterize the hydrodynamic status at the local element level of numerical model [47,48]. The modified Péclet number Pe_x and Pe_y represent the microscopic competitive relation between convective and diffusive heat transfer with a proximate resolution of CFD model.

$$Pe_x = \frac{v_x \cdot \delta x}{\alpha} \ , Pe_y = \frac{v_y \cdot \delta y}{\alpha} \tag{10}$$

$$\alpha = \frac{\lambda}{\rho C_p} \tag{11}$$

where δx and δy are the size of the control element which are equal to 10^{-3} m in this study, and v stands for the velocity within such element. The thermal diffusivity α was calculated by the temperature dependent physical properties of each element.

The bulk Richardson number (Ri_{bulk}) that indicates the overall competitive effect of buoyancy force and inertial force at the scale of the entire storage tank can be calculated by Eq. 12 [49].

$$Ri_{bulk} = \frac{g\beta(T_{in} - T_{out})H}{v_{in}^2} \tag{12}$$

Where g is the gravitational acceleration and β is the coefficient of thermal expansion of water. Ri_{bulk}>1 means that the temperature stratification is enough stable against the turbulence production shear whereas Ri_{bulk} <0.25 indicates unstable temperature stratification [14,50]. In between 0.25 and 1.0 is the transition range.

The gradient Richardson number ($Ri_{gradient}$) is also introduced in Eq. 13 [27,51].

$$Ri_{gradient} = \frac{|N^2(y)|}{S^2(y)} \tag{13}$$

Where N^2 is the squared Brunt-Väisälä frequency (also named as buoyancy frequency) and S^2 is the squared vertical shear production, calculated by Eq. 14 and Eq. 15, respectively.

$$N^2(y) = -\frac{g}{\rho_c}\frac{\partial \rho(y)}{\partial y} \tag{14}$$

$$S^2(y) = \left(\frac{\partial v_x}{\partial y}\right)^2 + \left(\frac{\partial v_y}{\partial y}\right)^2 + \left(\frac{\partial v_z}{\partial y}\right)^2 \tag{15}$$

By its definition, $N^2(y)$ is a measure of fluid stability to vertical displacements such as those caused by convection. For normal and stable thermocline, the value of N^2 is kept positive, meaning that the hot fluid is always located above the cold fluid. However, this value becomes negative when unexpected thermal overturning occurs, i.e., some streams of hot fluid are beneath the cold fluid. $S^2(y)$ is the sum of squared vertical shear rate tensor of the streamwise velocity in *x*, *y* and *z* coordinates [52]. The ratio of $N^2(y)$ and $S^2(y)$, the $Ri_{gradient}$, could be used to characterize the temeprature stratification at the local level [51].

The charging efficiency (η_{ch}) that presents the ratio of effective stored energy to the whole inlet energy can be calculated by Eq. 16.

$$\eta_{ch} = \frac{E_{in} - E_{out}}{E_{in}} = \frac{\int_0^t \dot{m}\, C_p(T_{in} - T_{out})dt}{\int_0^t \dot{m} C_p(T_{in} - T_c)dt} \tag{16}$$

Where $\dot{m}$ is the mass flow rate and E is the transported energy by inlet/outlet port.

The capacity ratio (σ) that indicates the ratio of real stored thermal energy to the maximum energy storage capacity of the tank is calculated by Eq. 17.

$$\sigma = \frac{E_{stored}}{E_{stored}^{max}} = \frac{E_{in}-E_{out}}{V_{tank}\,(Cp_{in}T_{in}\rho_{in}-Cp_cT_c\rho_c)} \quad (17)$$

Where V_{tank} (14.1 L) is the volume of inner fluid domain inside the tank.

2.6 Measurement uncertainty estimation

An uncertainty analysis was performed following the method of Moffat [53]. In our condition, as for η_{ch}, the independent variables include $\dot{m}$, T_{in} and T_{out}, while for the capacity ratio σ, ,an additional variable T_{ini} should be considered. Regarding the Ri_{bulk}, the independent variables are v_{in}, T_{in} and T_{out}.

The measuring accuracy of the temperature sensors (PT100) is $\pm(0.15 + 0.002T)$ °C while flow meters were calibrated for flow rate $0.05 - 5$ L min $^{-1}$ with the accuracy of 1%. For simplification of estimation, $\dot{m}$ is considered to be only dependent on the volume flow rate Q_{in}. By considering the HTF flow rate to be 1.0 L min^{-1}, T_{in} to be 333.15 K (60°C), T_{out} to be 293.15 K (20°C) and T_{ini} to be 293.15 K (20°C), and by taking into account the numerical integration errors, the relative uncertainty is estimated to be ±5% for η_{ch}, ±2% for σ and ±1.5% for Ri_{bulk}, respectively. . More details of the uncertainty analysis may refer to paper [54].

2.7 Comparison between CFD and PIV results

The hydrodynamic characteristics of a typical charging process has been investigated as a reference case for the comparison between the CFD and PIV results (Fig. 4). To do that, hot water at T_h =333.15 K and Q_{in} =1 L·min^{-1} was injected into the thermocline storage tank initially filled with cold water (T_c=293.15 K). Both the upper and bottom baffles have uniform orifices, their geometry and dimensions being given in section 3.1 and Fig. 6a.

Figure 4 shows a comparison on the evolution of the HTF velocity field in the interest area (downstream the upper baffle) at different charging times (*t*=100 s; 400 s and 700 s), obtained by PIV and CFD methods. Note that in experiments, an instantaneous velocity field captured by one PIV image would have certain small imperfections, such as the false signals due to air bubbles for example. For this reason, and to eliminate these imperfections, the velocity map by averaging 20 PIV images (5 s) before and after was treated to represent the instantaneous flow field at certain measurement moment shown in Fig. 4. Due to the existence of central orifice on the upper baffle, an inflowing hot water jet together with the progressive downward penetration can be clearly seen. With the initially momentum-dominated hot fluid flowing downwards, the inertia force is weakened by the vertical shear produced by the density difference at the interface of the injecting hot fluid and the surrounding cold fluid. The vertical velocity of the jet front decreases, and in the meanwhile, a certain portion of hot fluid is turned upward away from the centerline (transition regime). The phenomenon of jet entrainment is clearly shown in Fig. 4, i.e., two branches of the buoyant plume at left and right sides of the principal jet can be observed in both CFD and PIV pictures. The buoyant plumes first rise upwards due to the buoyancy force (in the buoyancy-dominated regime) until they touch the upper baffle, and then fall downward along the walls of the tank (the edgewise dispersion regime). All the flow regimes as schematized in Fig. 1 can be captured in the obtained numerical and experimental results.

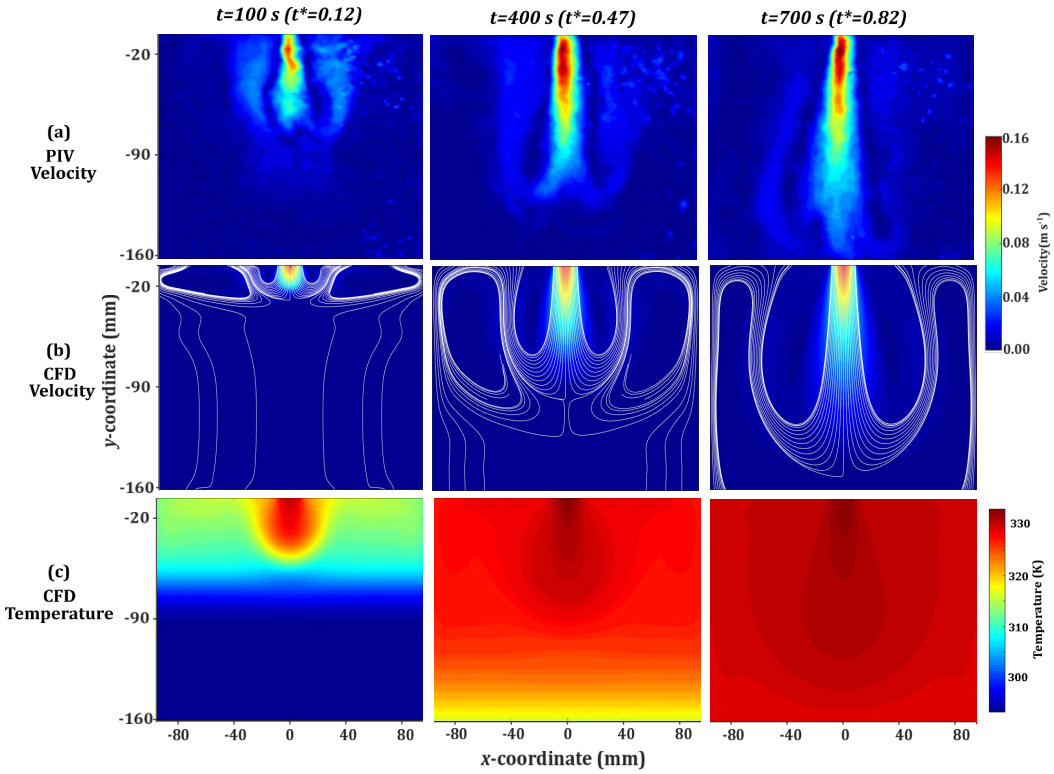

Fig.4. Characterization of the jet entrainment and buoyant plumes inside the SMT storage tank at different charging times. (a) velocity field obtained by PIV; (b) velocity field obtained by CFD; (c) temperature field obtained by CFD. Condition: $Q_{in} = 1$ L min^{-1}, T_h=333.15 K, T_c=293.15 K, baffles with uniform orifices.

Figure 4 also shows that the calculated transient temperature fields and velocity fields are closely related. The inflowing thermal jet advances along with the thermocline moving downward during the charging process.

Figure 5 compares the jet penetration length (h_j), as a function of charging time, obtained by the CFD and PIV methods. Recall that h_j quantifies the longest extended length of the thermal jet front from the top inlet port of the storage tank to where the vertical velocity component becomes zero (v_y=0) at the centerline. In practice, the position of this neutral point is identified as soon as the negative v_y turns to be positive, as will be displayed in Fig. 8a (zone C) and Figs. A1-A3. The capture of h_j value is straightforward in CFD post-processing. But for PIV measurement, since the instantaneous image is not representative, this value has been determined by averaging a total of 50 images before and after the certain time t. The same trend may be observed from both the CFD simulation and the PIV measurement: the h_j value increases monotonously with the charging time t. It reaches about y=-160 mm at t =700 s which is near the bottom border of the visualization window. The difference of the h_j values (between the CFD and PIV) ranges from 33.9 mm (31.0%) to 24.5 mm (12.1%) when the charging time t increases from 50 s to 650 s.

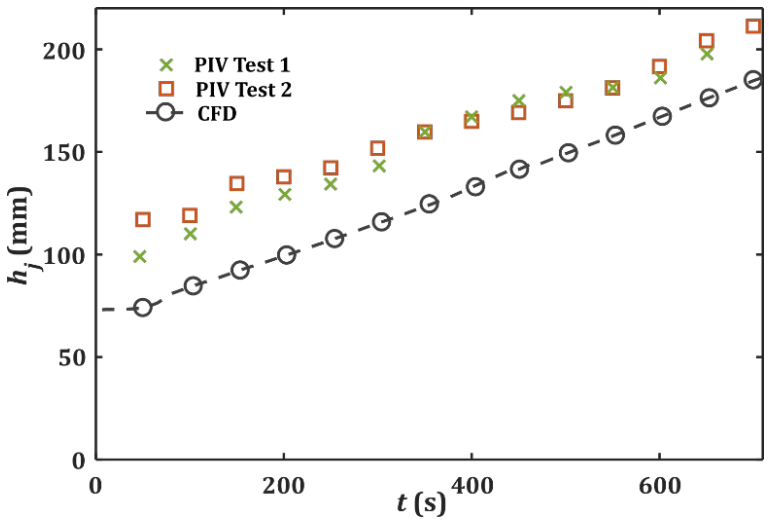

Fig. 5. Comparison on the length of penetration (h_j) as a function of charging time obtained by PIV and CFD methods. Condition: $Q_{in} = 1$ L min^{-1}, T_h=333.15 K, T_c=293.15 K, baffles with uniform orifices.

This deviation can be derived equally from the associated uncertainties or intrinsic errors of the PIV and CFD methods. Firstly, despite the careful pre-heating step for each experiment, the small perturbation of the (initial) inlet condition (flow rate, temperature) still exit due to the needed response time of the 3-way valves, rendering a relatively larger difference of h_j at the beginning stage of the charging. Secondly, the experimental h_j value has been obtained by averaging 50 PIV images to eliminate false signals and measurement imperfections. The use of the averaged h_j value of a certain time period (12.5 s) instead of the instantaneous value may also cause the deviation from the real penetration length. Thirdly, the camera-laser-tank calibration procedure for PIV, although carefully done before each measurement, may still cause the small deviation on the visualized position. Fourthly, besides other assumptions and simplifications made for the CFD model (e.g., neglected heat loss, k-ε turbulent model, etc.), the use of normal to the boundary velocity profile at the inlet port rather than the "closer-to-the-reality" parabolic velocity profile will cause an underestimation of the h_j value with respect to the experimental data.

More detailed comparison on the PIV velocity profiles (velocity magnitude, *x* and *y* components) at different time and space coordinates can be found in Appendix A of this paper, clearly showing that CFD and PIV results are in acceptable agreement. In brief, the transient velocity fields can qualitatively showcase the flow regimes of the jet entrainment and well predict the h_j value and its increasing tendency with charging time. In this regard, the CFD model and the associated parameters used in the simulation are considered to be adequate to describe the evolution of fluid flow profiles and thermocline behavior used subsequently for optimizing the size distribution of orifices on the upper baffle.

3. Optimization of the orifice baffle for enhanced stratification: the CFD results

This section presents the numerical results obtained on the optimization of the upper orifice baffle. Firstly, the optimization algorithm is briefly introduced. Then the fluid flow and temperature characteristics as well as the dynamic thermocline behaviors before and after the optimization will be compared and discussed in detail.

3.1. Optimization algorithm

The optimizing algorithm has been developed in a way that the size distribution of perforated orifices on the baffle is adjusted to minimize the volume of the thermocline in the storage tank. This method has been proposed and developed in 2D [43] and extended to asymmetry 2D for the design and optimization of ring-opening plate distributors in our earlier study [29]. But it is applied in the first time to a real 3D orifice distributor being installed into a lab-scale thermocline storage tank. Here only the basic principles of the optimization algorithm and some key steps are introduced. More details about the algorithm itself, e.g., the optimization criterion, the numerical tested cases, the influencing parameters, etc. may refer to [43].

The basic idea of optimization is to adjust the sizes of orifices on the baffle so that the thermal front could pass through every orifice at almost the same time. Here the passage time t_i is defined as the time interval between t_0 (charging start) and the moment when the thermal front (T_{80} in this study) just traverses the i^{th} orifice on the upper baffle. In other words, it corresponds to the moment when the mean fluid temperature in the i^{th} orifice is equal to T_{80}.

Note that the temperature threshold values T_{80} and T_{20} are used in this study to define the borders of the thermocline zone, their values being calculated by Eq. 18.

$$T_{80} = T_c + 80\% \times (T_h - T_c)$$
$$T_{20} = T_c + 20\% \times (T_h - T_c) \tag{18}$$

The temperature value is also normalized for simple interpretation and comparison:

$$T^* = \frac{T - T_c}{T_h - T_c} \tag{19}$$

The dimensionless thermocline volume V^* is defined as the volume proportion of the storage tank occupied by the thermocline zone [T_{20}; T_{80}].

$$V^* = \frac{V_{[T20;T80]}}{V_{tank}} \tag{20}$$

The mean passage time for all the orifices can be calculated Eq. 21.

$$\bar{t} = \frac{\sum_{i=1}^{N} t_i}{N} \tag{21}$$

The optimality criterion is written as:

$$t_i = \bar{t}\ (i = 1, 2, \ldots N) \tag{22}$$

This suggests that the thermally piston flow could be realized when the passage times (t_i) for all orifices are identical.

An iterative program is written such that the surface area of the i^{th} orifice (s_i) is modified according to the deviation of its passage time to the mean value ($t_i - \bar{t}_i$). Specifically for j step, the s_i will be reduced for step $j+1$ if $t_{i,j}$ is found smaller than $\bar{t}_{i,j}$. Otherwise, s_i will be enlarged for step $j+1$ if $t_{i,j}$ is observed larger than the mean $\bar{t}_{i,j}$ at step j.

$$\Delta s_{i,j} = s_{i,j+1} - s_{i,j} = \gamma\left(t_{i,j} - \bar{t}_j\right) \tag{23}$$

Where γ is an adjusting factor chosen to ensure a fast and stable convergence.

$$t_{manifold} = \frac{V_{manifold}}{Q_{in}} \tag{24}$$

Where $V_{manifold}$ is the volume of upper/bottom manifold (1.33 L).

The dimensionless charging time t^* is defined as the ratio of the instantaneous charging time to the theoretical residence time to fill up the storage tank by an ideal plug flow at a constant flow-rate.

$$t^* = \frac{t}{\frac{V_{tank}}{Q_{in}}} \tag{25}$$

3.2 Optimization results

Uniform orifice configuration was used as the reference case to start the optimization (step 1), the arrangement of orifices being shown in Fig. 6. The ratio between the sum of whole opening surfaces and the inner cross-section surface area of tank, also named as the baffle porosity, is equal to 0.20. Considering such orifices arrangement for both upper and bottom baffles and the symmetry character of the storage tank geometry, one-eighth of the body has been used for simulation and optimization. Note that only the upper baffle was optimized for the charging operation while uniform orifice bottom baffle was always used in this study.

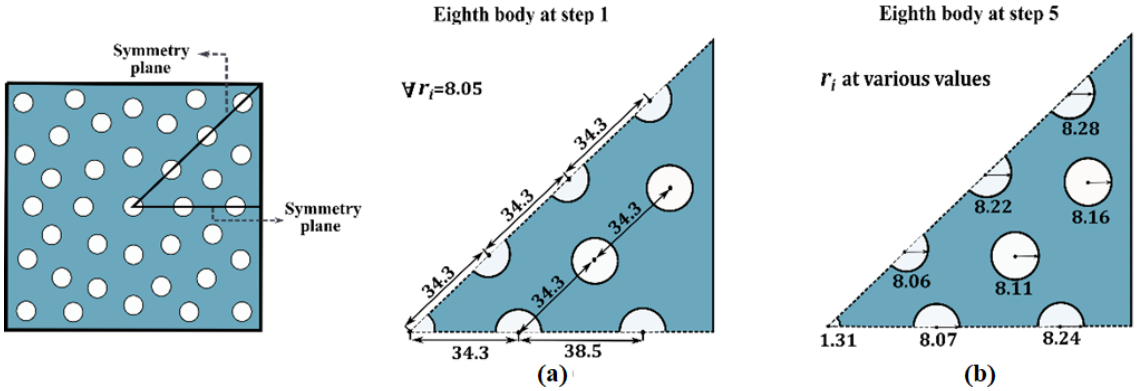

Fig. 6. Geometry and dimension details of the upper orifice baffle tested in this study. (a) initial uniform orifice configuration; (b) optimized orifice configuration (Unit: mm). Condition: Q_{in} = 1 L min^{-1}, T_h=333.15 K, T_c=293.15 K.

It can be observed that after optimization, the size of the central orifice is largely reduced from 8.05 mm to 1.31 mm while other orifices are all enlarged to a similar size (8.06-8.22 mm). Based on the constraint of constant baffle porosity in the optimization algorithm, the passage surface area of the initial central orifice is allocated to the orifices situated on the edge of the baffle, guiding the hot fluid to occupy the whole upper manifold before crossing through the (non-uniform sized) orifices. The variation trend is in line with the 2D numerical results obtained in our earlier study [43].

Figure 7 demonstrates the time evolution of the dimensionless thermocline volume V^*. It can be observed that the rising rate, the maximum value of V^* and the corresponding reaching time are different for different optimization steps. For step 1 and 2, the *V** curve still continues to rise after the $t^*_{manifold}$ time, indicating the mixing of the injecting hot water with the environment cold water in the middle storage region of the tank below the upper baffle. The volume of the thermocline expands to a peak value and then tends to decline and stabilize. From step 3 on, the flow mixing is by and large restricted in the upper manifold, shown by the reaching of *V** peak value at the $t^*_{manifold}$ moment. In other words, the V^* curve seems to be flattened from one optimization step to the next, while the temperature stratification below

the upper baffle becomes less disturbed by the inflowing thermal jet. Especially for the optimized configuration (step 5), the V^* curve climes to reach the shift point at t^*=0.097, then remains almost stable afterward. This implies that the optimized OBD helps establish a more stable thermocline between the hot and cold fluids, and manage its (almost) undisturbed advance over time.

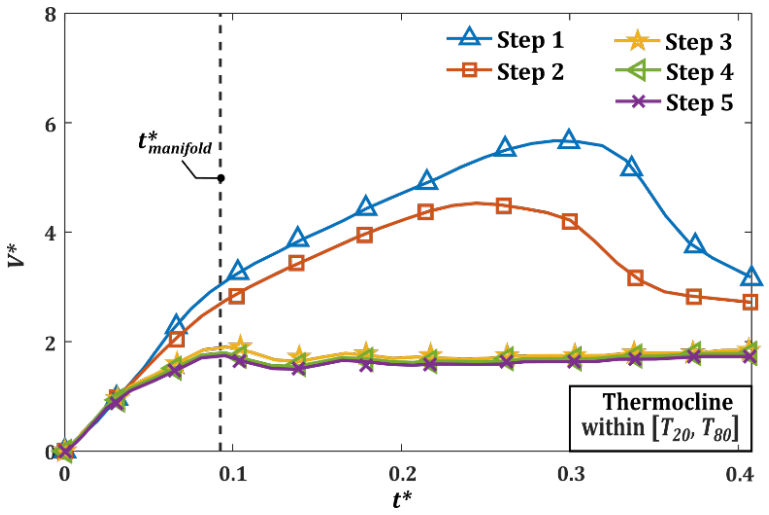

Fig.7. Time evolution of the dimensionless thermocline volume V^*. Condition: Q_{in} = 1 L·min^{-1}, T_h=333.15 K, T_c=293.15 K.

The comparison on the V^* value clearly shows that the temperature stratification can be better maintained by optimizing the OBD using the proposed algorithm. Nevertheless, the effect of conjugated fluid flow and heat transfer on the thermocline evolution is still masked. A close look at the local velocity and temperature profiles is thereby necessary to provide additional insights on the jet entrainment phenomenon and buoyant plumes, which is detailed in the following sub-section.

3.3 Comparison on the velocity and temperature profiles

Figure 8 shows the contours of the velocity magnitude in half of the interest area (below the upper baffle) for the uniform orifice configuration (Fig. 8a) and for the optimized orifice configuration (Fig. 8b). Local snapshots with adaptive enlarged ratio of each have been extracted and displayed on the figure, showing the amplified velocity vectors in some typical areas. Note that the instantaneous flow fields at $t^*_{manifold} = 0.0927$ are shown and compared here, corresponding to the theoretical moment when the upper manifold is fully occupied by an ideal plug-flow of the incoming hot water (Q_{in}=1 L·min^{-1}).

From Fig. 8(a), it can be observed that the injecting hot fluid passes easily through the (large) central orifice, pushing the cold fluid far away from the upper baffle. The momentum-dominated thermal jet has large v_y component at first and then gradually exhausts. This is because the existing density difference between the hot jet and the surrounding cold fluid induces the buoyancy force, indicated by the upward velocity vectors along the vertical central line as shown in zone C. At a certain penetration length h_j, the buoyancy force, the inertia force and the gravity are balanced and offset, the v_y component being zero at this point.

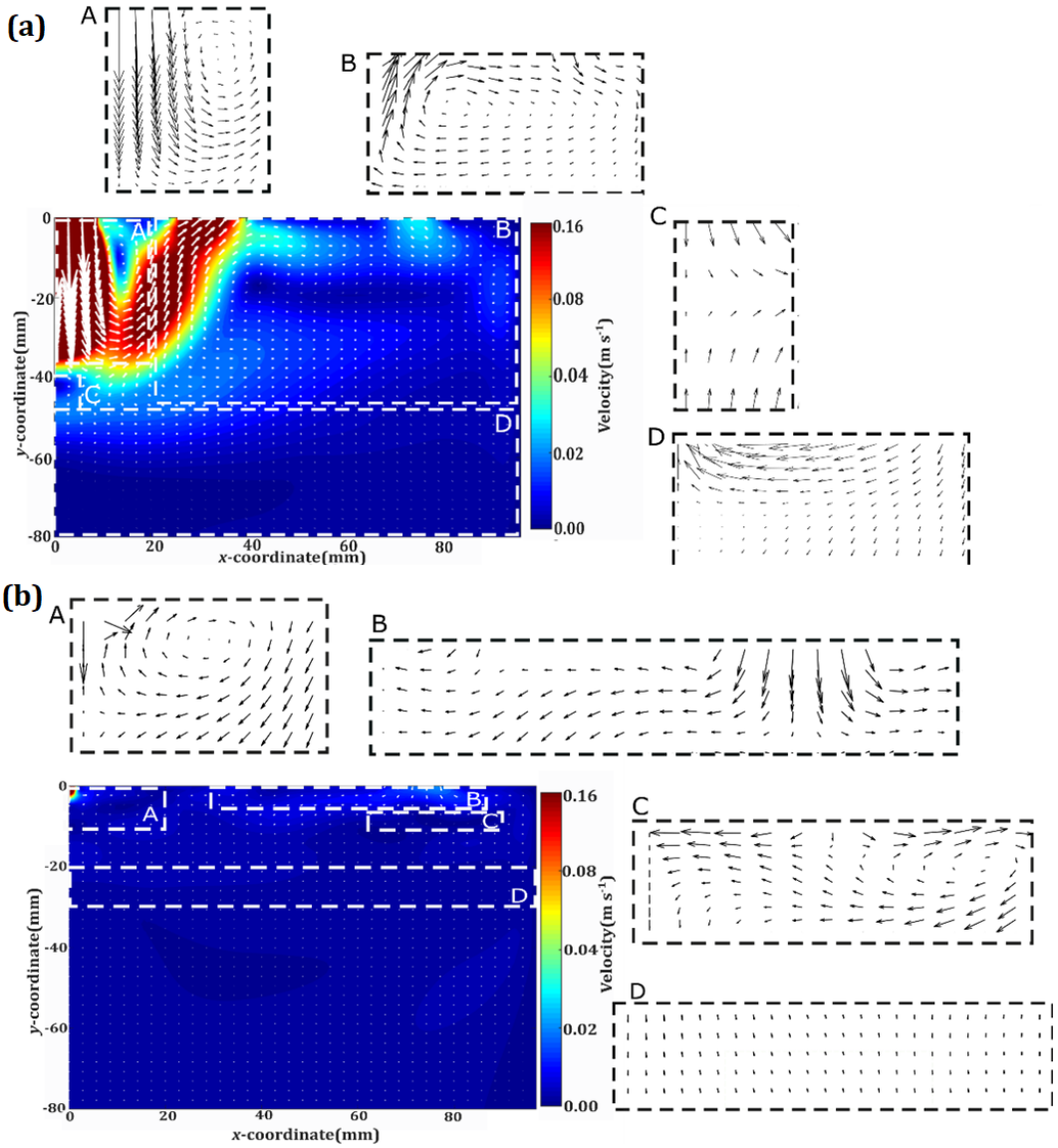

Fig. 8. Velocity vectors superimposed over velocity contour at half of the interested area of the SMT tank at $t^*_{manifold} = 0.0927$ (79.5 s). (a) initial uniform orifice baffle; (b) optimized orifice baffle. Condition: $Q_{in} = 1$ L min^{-1}, T_h=333.15 K, T_c=293.15 K.

The produced velocity shear yields the entrained flow that changes the advancing direction. A good part of the fluid flow has thus been brought away from the axial direction, but risen back to the upper baffle in the form of plume. The temperature of the rising plume falls down by mixing with the surrounding cold fluid. When the plume touches the upper baffle, a small part of the fluid flow re-enters the upper manifold through the orifices (upward velocity vectors shown in zone B) while the main stream goes in horizontal (x) direction towards the lateral walls of the storage tank and bounces back (zones B and D). Vortices of different sizes can be observed: one between the inflowing jet and the rising plume branch (zone A) and another between the rising plume and the edge (zone B). The latter one stretches over a large horizontal distance, the v_x component of the fluid flow being more important.

The existence of various vortices and flow recirculating zones enhances the temperature mixing, as shown in Fig. 9a. Actually for an ideal plug-flow condition, the hot front would just cross through the upper baffle at $t^*_{manifold}$ ($t = 79.5$ s), i.e., at $y = 0$ mm in Figs. 8 and 9. But for the initial uniform OBD,

the thermocline goes much deeper and reaches $y = -49.5$ mm. The temperature stratification is largely degraded due to the momentum-dominated inflowing jet (through the central orifice) as well as the rising plumes. Consequently, the thermocline zone has already occupied a large volume of the middle storage zone at $t^*_{manifold}$ moment.

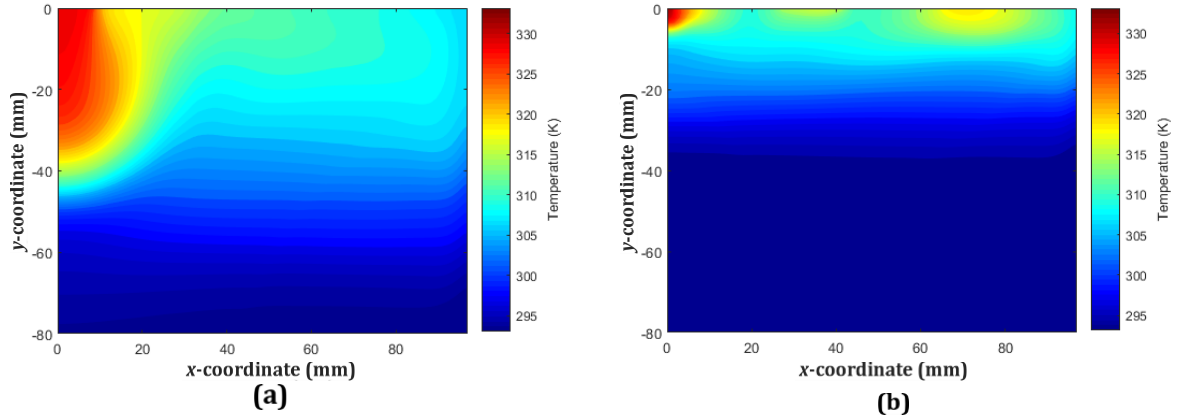

Fig. 9. Temperature contour of the half interest area at $t^*_{manifold}$. (a) initial uniform OBD; (b) optimized OBD. Condition: $Q_{in} = 1$ L min^{-1}, T_h=333.15 K, T_c=293.15 K.

From the velocity contours and vectors shown in Fig. 8(b), one may find that a calmer flow pattern can be achieved with the optimized upper OBD. Since the surface area of the central orifice was significantly reduced (others were enlarged), the hydraulic resistance of the central orifice facing the inlet port is thereby much higher. More hot fluid is guided toward the orifices on edge of the upper manifold (zone B). The thermal jet through the central orifice penetrates only a very small distance (zone A). The rising plumes are hardly visible and the generated vortices are much smaller (zones A and C), the hot and cold fluids being less mixed. A stable and uniform velocity profiles (upward v_y component) are formed at $y < -20$ mm (zone D and below) at $t^*_{manifold}$. The temperature cartography shown in Fig. 9b also indicates that the thermocline becomes more flattened and thinner compared to that of the initial uniform orifice case (Fig. 9a).

3.4 Convective vs. diffusive heat transfer: $Ri_{gradient}$ and Pe number

The $Ri_{gradient}$ number and the element Pe number are calculated and discussed here, so as to provide additional insights on the stratification degradation due to the effect of convective or diffusive heat transfer mechanisms. Figure 10 shows the N^2, $S^2$and $Ri_{gradient}$ curves at different depths of the interest area at $t^*_{manifold}$.

Negative values of N^2 $(y = -10\ mm)$ may be found near the centerline (x between 10 and 20 mm) for steps 1 and 2, implying that the thermal overturning ($\frac{\partial T(y)}{\partial y} > 0$) occurred in these areas. This is caused by an eddy between the downward jet from the central orifice and the rising plume, as mentioned earlier in Fig. 8(a). The value of S^2 in this eddy zone is also very high, indicating the large shear stress induced by the central inflowing jet. The thermal overturning yields the degradation of temperature stratification, characterized by $Ri_{gradient} < 0.25$ shown in Fig. 10 for steps 1 and 2. Another subcritical peak $(Ri_{gradient} < 0.25)\ at\ y = -10\ mm$ could be identified at x=80 mm, corresponding to the locations where the vortices are generated as shown in Fig. 8a.

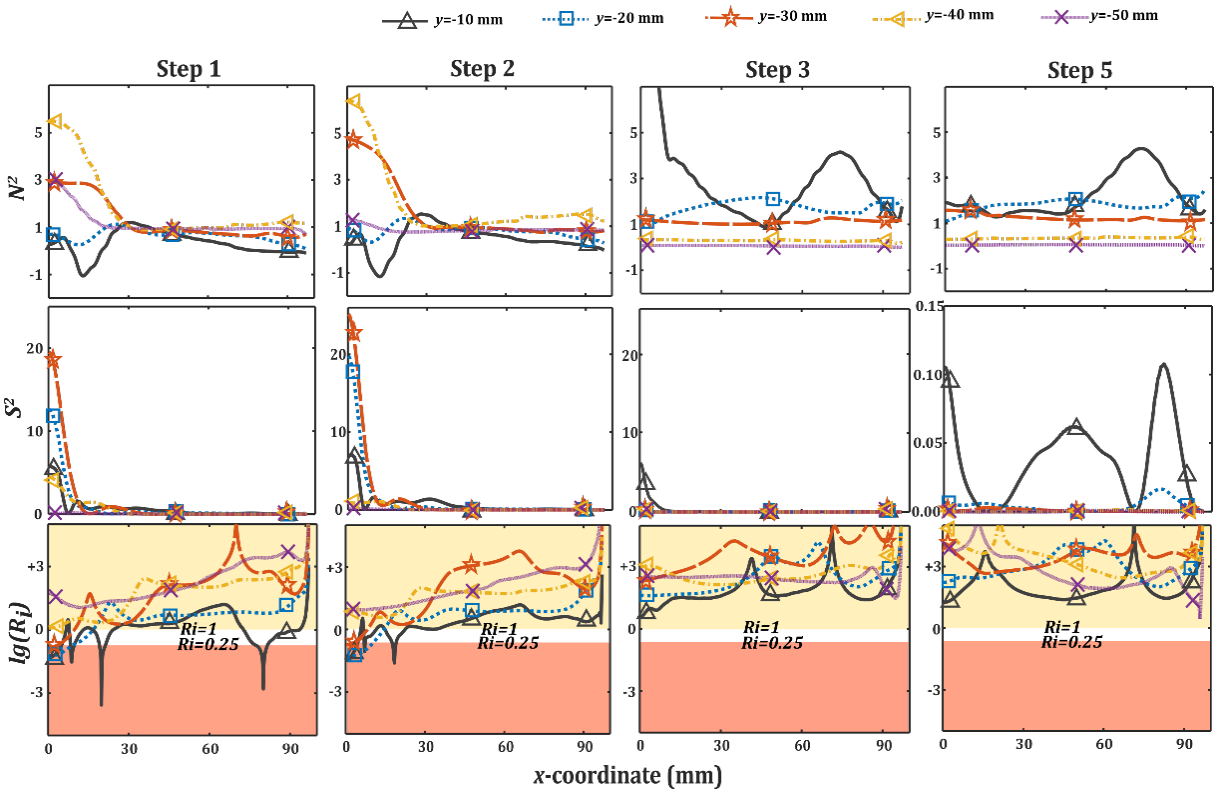

Fig. 10. Squared Brunt–Väisälä frequency N^2, squared vertical shear production S^2 and the gradient Richardson number $Ri_{gradient}$ at $t^*_{manifold}$ for different optimization steps. Condition: Q_{in} = 1 L min^{-1}, T_h=333.15 K, T_c=293.15 K.

The values of N^2 become all positive after step 3, implying that all vortices that cause the thermal overturning have been eliminated. Moreover, N^2 value could be kept at 0 at the position $y = -50\ mm$, indicating that the cold fluid is calmly maintained at $t^*_{manifold}$.

The analysis of the $Ri_{gradient}$ number (as well as N^2 and S^2) clearly shows that the temperature stratification can be better maintained from one optimization step to the next. At step 5, $Ri_{gradient}$ curves at different *y* positions are all higher than 1. Stable thermocline in the middle storage zone has thereby been achieved with the help of the optimized upper OBD.

From the heat transfer point of view, it is also interesting to examine the competitive relationship between convection and diffusion, which are two mechanisms that degrades the temperature stratification. In this regard, the x and y components of the element Pe number (Pe_x and Pe_y) at $t^*_{manifold}$ for both the initial uniform OBD and the optimized OBD are calculated and compared in Fig. 11. Note that Pe_x and Pe_y values are plotted in logarithmic scale, with its upper and lower range at a certain *y*-coordinate and the point for the mean value.

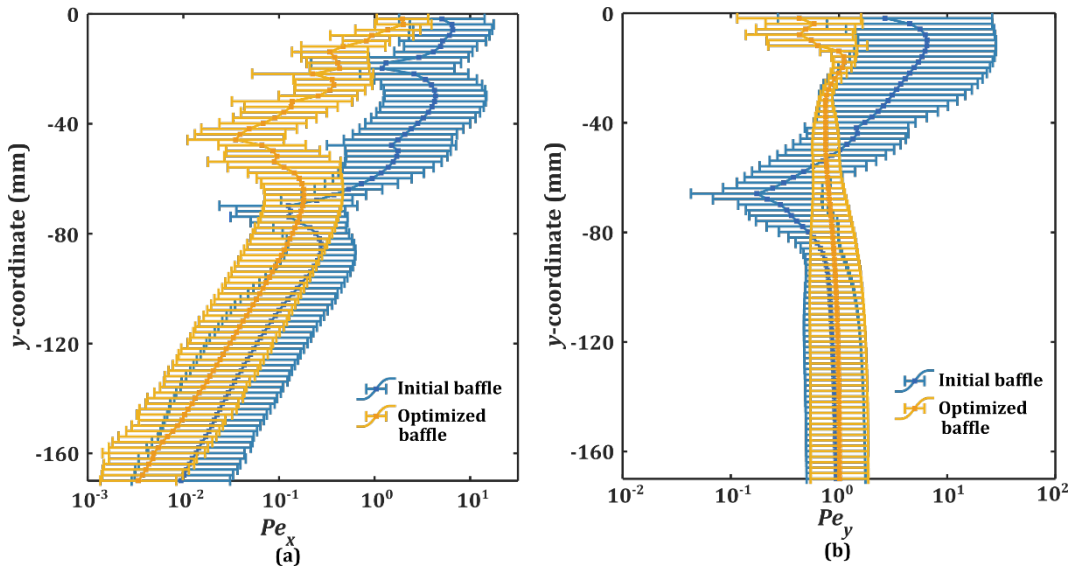

Fig. 11. Comparison on the element Pe numbers at $t^*_{manifold}$ for the initial uniform OBD and the optimized OBD. (a) Pe_x; (b) Pe_y. Condition: $Q_{in} = 1$ L min^{-1}, T_h=333.15 K, T_c=293.15 K.

For the initial uniform OBD (blue curve), Large Pe_x and Pe_y values can be observed in zone -50 mm< y <0 mm, indicating the strong fluid mixing and the convection-dominated heat transfer. This is in line with the local velocity and temperature profiles analyzed and discussed in the above section 3.3. The thermocline zone has significantly expanded in this area at $t^*_{manifold}$. A diffusion transport dominated zone may be observed at -90 mm< y<-50 mm, indicated by the value of Pe_x and Pe_y<1. This is also coherent to the earlier mentioned neutral buoyancy zones C and D shown in Fig. 8a. Below y=-90 mm, the Pe_x value becomes very small mainly because of the negligible v_x. In contrast, Pe_y values stabilizes around 1, indicating the balanced convective and diffusive heat transfer when the cold fluid progresses.

For the optimized OBD (orange curve), the convective transport is dominating within only a thin zone (-10 mm< y <0 mm) just beneath the upper baffle. Since Pe_x value becomes smaller than 1 below y=-10 mm, the diffusion becomes the dominating heat transfer mechanism along the x direction (eddy advection eliminated). Likewise, the balanced convective and diffusive transport is achieved at y <-30 mm, indicated by Pe_y=1 in Fig. 11b.

In brief, the optimized orifice configuration, in comparison with the initial uniform orifice configuration, could yield the diffusion-dominated transport along the *x*-direction and a balanced convection/diffusion transport along the y-direction at a much smaller depth of the storage tank. Both effects help alleviate the fluid mixing thus enhance the temperature stratification (thinner thermocline zone).

4. Influences of operating parameters on the thermal jet propagation and on the thermal performance of the SMT storage tank: experimental results

The numerical results presented in the above section has demonstrated that the optimization algorithm is really effective in maintaining the temperature stratification and manage the undisturbed thermocline advance. Based on these encouraging findings, the optimized OBD as well as the initial uniform OBD were fabricated and installed in the lab-scale storage tank. Charging experiments were then performed

under various inlet flow-rate and inlet temperature conditions. Measuring the local velocity profiles by the PIV method as well as the inlet/outlet temperature evolutions of the storage tank by RTD sensors will further reveal and confirm the thermal performance improvement of the SMT storage tank by using the optimized OBD. In particular, the influences of the injecting flow rate and the temperature difference (between T_h and T_c) on the thermal jet entrainment/penetration and on the thermal performances (indicated by Ri_{bulk} number, η_{ch} and σ) will be addressed, providing guideline for the design and operating of SMT storage tanks for different applications.

4.1 Effect of the injecting flow rate

The injecting flow rate (Q_{in}) is a key parameter that determines the flow patterns inside the SMT storage tank. Higher Q_{in} will result in higher inertial force of the jet, thus promotes the mixing. But the thermocline decay has also been observed at very low Q_{in}, mainly due to the thermal diffusion [29,55]. The competition between the effect of mixing and thermal diffusion may result in an optimal Q_{in}.

The charging experiments were performed for the SMT storage tank equipped with either the initial uniform OBD or the optimized OBD, at an injecting flow-rate of Q_{in}=0.3-1.5 L·min^{-1} and a temperature difference of 40 K (T_h=333.15 K; T_c=293.15 K). Figure 12 gives a comparison on the velocity profiles of the interest area (initial uniform OBD) for different injecting flow rates, captured by PIV at t^*=0.4 and t^*=0.8, respectively. It can be observed that the higher flow rate with larger inertia force provokes the longer penetration depth (h_j) at the same t^*. For example, the front of thermal jet at Q_{in}=0.3 L·min^{-1} touches y=-50 mm at t^*=0.4 whereas at Q_{in}=1.5 L·min^{-1}, it has already crossed over the lower border of the visualization window (y=-160 mm).

In the meanwhile, buoyant plumes can be observed at both sides of the central inflowing jet. The larger the Q_{in}, the thicker the rising branches as displayed in Fig. 12. The higher mass of hot fluid is injected per unit time at high Q_{in}, and proportionally a higher amount is deflected and change the direction (compared to low flow rate condition), occupying the larger volume of the storage tank in the form of rising plumes. At each Q_{in}, the front of thermal jet penetrates deeper with the increasing charging time. This is because the vortices and flow recirculation enhance the heat transfer so that the temperature difference becomes smaller between the inflowing jet at the central line and its surroundings. The buoyancy force is thereby reduced due to the smaller density difference.

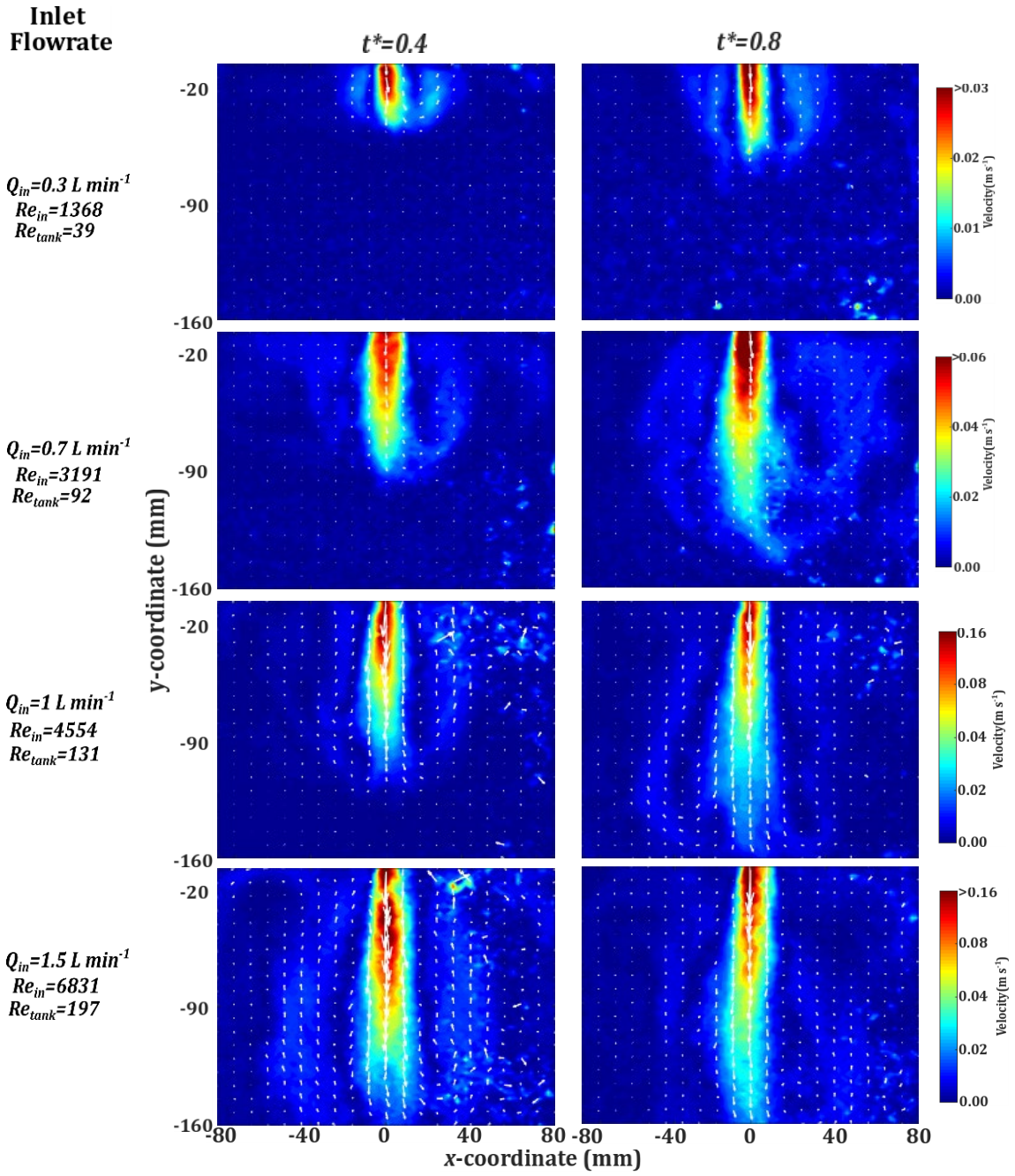

Fig. 12. Velocity profiles of the interest area measured by PIV for different injecting flow-rate at t^*=0.4 and t^*=0.8. Condition: T_h=333.15 K, T_c=293.15 K, initial uniform OBD.

Figure 13a shows the bulk Richardson number (Ri_{bulk}) versus t^* under different Q_{in} conditions. The Ri_{bulk} curves for different Q_{in} are all kept in a plateau over a certain period of time during which the thermocline doesn't influence the HTF outlet temperature ($T_{out} = T_c$) at the bottom port of the storage tank. The Ri_{bulk} curves of the initial uniform OBD begin to fall at different t^*: t^*=0.4 for Q_{in}=1.5 L·min^{-1}, t^* =0.7 for Q_{in}=1.0 L·min^{-1}, and about t^* =0. 8 for Q_{in}=0.7 and 0.3 L·min^{-1}. The convection heat transfer is smaller at lower Q_{in}, ensuring a better temperature stratification. This can also be confirmed by the consistently higher Ri_{bulk} values of Q_{in}=0.3 L·min^{-1} than those of the other Q_{in}. For the optimized OBD case, very similar trend can be observed from Fig. 13a, except that the falling points of Ri_{bulk} curve are all delayed until t^*=0.9.

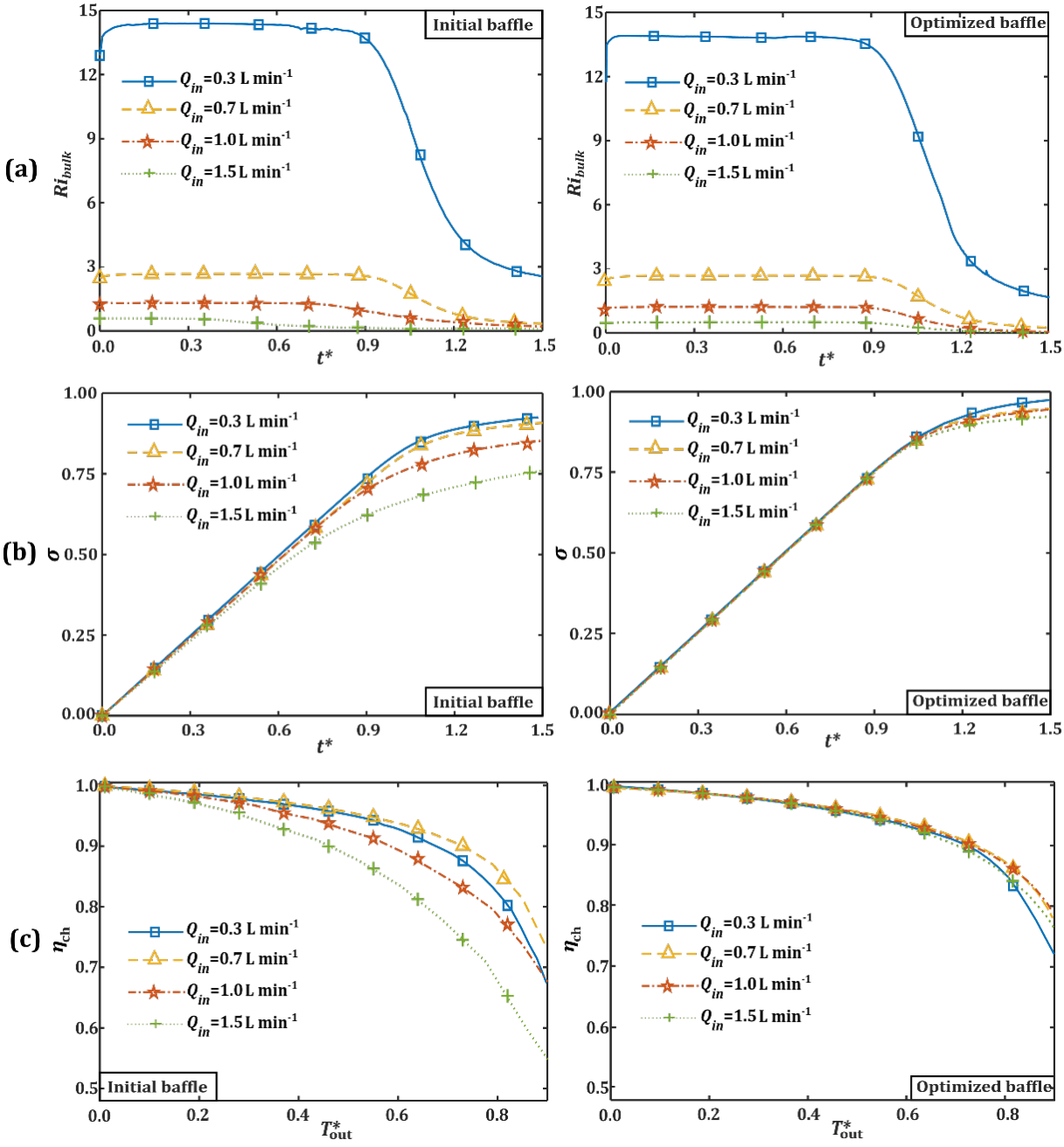

Fig. 13. Comparison on the thermal performance of the SMT storage tank for different inlet flow rates, with initial uniform OBD or optimized OBD. (a) bulk Richardson number Ri_{bulk} versus dimensionless charging time t^*; (b) capacity ratio σ versus t^*; (c) charging efficiency η_{ch} versus cut-off temperature T^*_{out}. Condition: T_h=333.15 K, T_c=293.15 K.

Figure 13b shows the storage capacity (σ) curves versus t^* under different Q_{in} conditions. Recall that this parameter indicates the ratio of real stored thermal energy to the maximum energy storage capacity of the storage tank. For the initial uniform OBD case, the σ curve of a certain Q_{in} first rapidly climes and then tends to stabilize. At t^*=1.5 the σ value for Q_{in}=0.3 L·min^{-1} reaches 0.92 while that for Q_{in}=1.5 L·min^{-1} approaches 0.77, still far from the fully charged status (σ =1). For the optimized OBD case in contrast, the four σ curves are almost overlapping over the charging time, reaching 0.94 at t^*=1.5. The departure from the ideal fully charged status is partly due to the heat loss to the environment since the SMT storage tank was not insulated during the PIV experiments which will be further discussed below.

Figure 13c shows that the charging efficiency η_{ch} decreases with the increasing outlet temperature T^*_{out} (also called the cut-off temperature). For the initial uniform OBD case, the higher Q_{in} results in the lower η_{ch}, except for the curve of Q_{in}=0.3 L·min^{-1} which falls between that of Q_{in}=0.7 L·min^{-1} and 1.0 L·min^{-1}. Although the calm and flattened thermocline can be largely maintained for almost the whole charging time at Q_{in}=0.3 L·min^{-1} (as indicated by the high Ri_{bulk} number shown in Fig. 13a), the real charging time to reach the fully charged status becomes very long. As a result, the amount of heat transferred by the thermal diffusion (between the hot and cold fluids) and the heat loss to the environment (due to the lack of insulation) become non-negligible, resulting in the smaller η_{ch} values at a high T^*_{out}. This also confirms the existence of an optimal Q_{in} as reported in the literature. But in real-world application, the Q_{in} and the cut-off outlet temperature should be coordinated and determined together so as to guarantee a high charging/discharging efficiency of the process. Regarding the optimized OBD case, the η_{ch} values at a certain Q_{in} are consistently higher than its counterpart (initial uniform OBD). The three η_{ch} curves (Q_{in}=0.3; 0.7 and 1.0 L·min^{-1}) are again almost overlapping, except for the Q_{in}=0.3 L·min^{-1} curve which falls rapidly after $T^*_{out} = 0.7$ due to the reason explained above.

In conclusion, a low Q_{in} is generally favorable to achieve a high σ and η_{ch} when the inlet diffuser is less performant. This is in line with the findings of our earlier study [29]. By using the optimized OBD, the global thermal performance of the storage tank could be improved, and the impacts of Q_{in} (momentum-dominated thermal jet) are by and large mitigated under our tested conditions.

4.3 Effect of working temperature difference

The effect of the working temperature difference ($\Delta T = T_h - T_c$) on the global thermal performance of SMT storage tank has been subjected to extensive numerical and experimental studies, but controversy still exists in the literature. Some researchers reported the positive effect of larger ΔT on the charging/discharging efficiency (e.g., [21,56]), while others (e.g., [57,58]) found that the temperature stratification might be degraded more easily with a larger ΔT. Therefore, investigation is still needed to reveal how this parameter impacts the local velocity (and temperature) profiles and on the global thermal performance of the SMT storage tank, especially by examining the real-time penetration characteristics of the thermal jet.

Additional charging experiments were performed under different working temperature differences ($\Delta T = 30; 40; 50$ K; $T_c = 293.15$ K) for the SMT storage tank equipped with either the initial uniform OBD or optimized OBD. The velocity profiles of the interest area (initial uniform OBD) at t^*=0.4 and 0.8 recorded by PIV are displayed in Fig. 14. Although the inertia force is the same (Q_{in}=1 L·min^{-1}), the penetration and propagation of the thermal jet clearly differ when ΔT changes. The larger buoyancy force due to the higher ΔT (T_h= 343.15 K in this study) can better balance out the inertia force of the inflowing jet, the h_j being thereby smaller. With the charging time proceeds, the front of thermal jet penetrates deeper due to the smaller buoyancy force, i.e., smaller temperature difference between the jet and the surrounding. In contrast, the penetration length for ΔT =30 K (T_h=323.15 K) is always the largest among the tested conditions, the upper region of storage tank being quickly occupied by the intermediate temperature fluid due to the strong convective heat transfer.

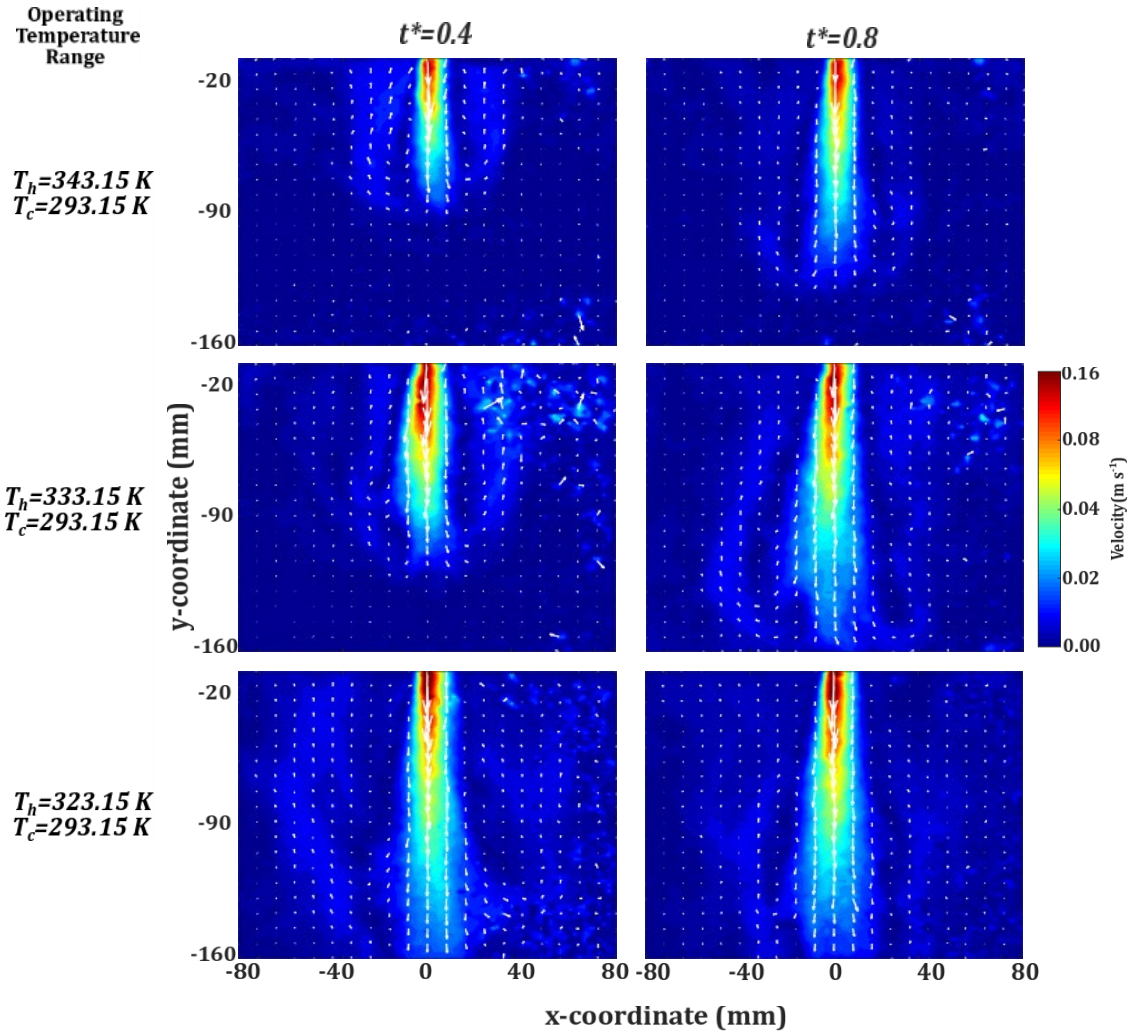

Fig. 14. Velocity profiles of the interest area for different working temperature differences at t^*=0.4 and t^*=0.8. Condition: Q_{in} = 1 L min^{-1}, initial uniform OBD

The global performance indicators of the SMT storage tank under different T_h conditions, with initial uniform OBD or optimized OBD, are presented in Fig. 15 and briefly commented below. The Ri_{bulk} curves shown in Fig. 15a indicates better temperature stratification under the higher ΔT condition, in agreement with the observation from Fig. 14. Figures. 15b and 15c show the similar trend, i.e. relatively better thermal performance, indicated by higher σ and η_{ch} values that can be achieved with a larger ΔT when the inlet flow diffuser is less performant (initial uniform OBD case).

When using the optimized OBD, the impact of ΔT on the thermal performance of the storage tank seems negligible, indicated by almost overlapping curves of σ and η_{ch} in Figs. 15b and c.

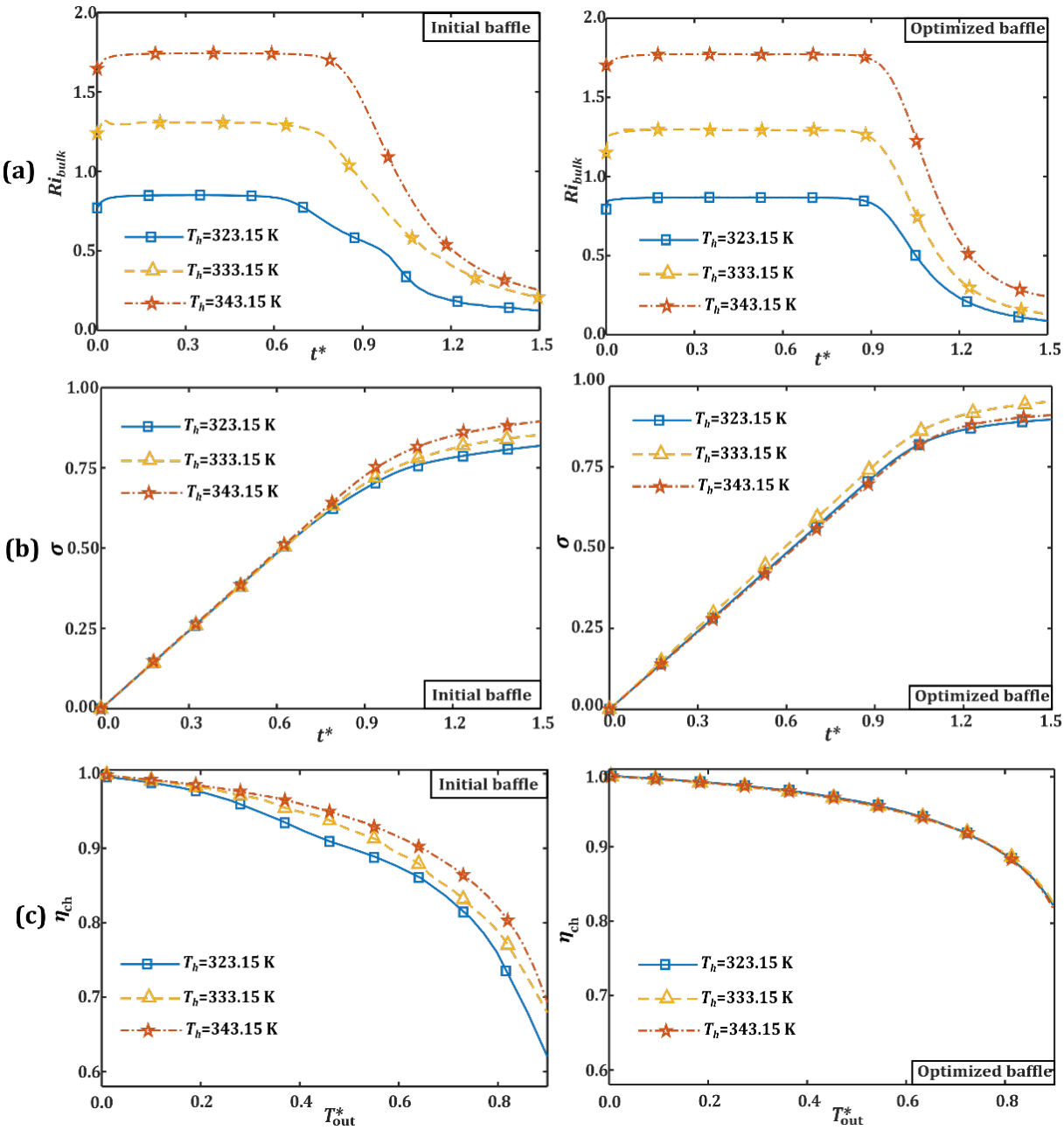

Fig. 15. Comparison on the thermal performance of the SMT storage tank for different working temperature differences, with initial uniform OBD or optimized OBD. (a) bulk Richardson number Ri_{bulk} versus dimensionless charging time t^*, (b) capacity ratio σ versus t^*; (c) charging efficiency η_{ch} versus cut-off temperature T^*_{out}. Condition: $Q_{in} = 1$ L min^{-1}.

A close look at the evolution of velocity profiles using the optimized OBD is illustrated in Fig. 16, under different ΔT conditions. Recall that the surface areas of the orifices have been reallocated by running the optimization algorithm, equalizing the passage times of the hot front for all the orifices. The flow rate passing through the orifices has also been redistributed, i.e., the central momentum-dominated jet is no longer existing and the velocity magnitude is largely reduced. Some parameters of the high speed camera and the laser of the PIV facility have thereby been readjusted to better observe and capture this relatively small velocity magnitude (e.g., maximum velocity at 8 × 10^{-3} m·s^{-1} on Fig. 16 vs. 0.16 m·s^{-1} on Fig. 14).

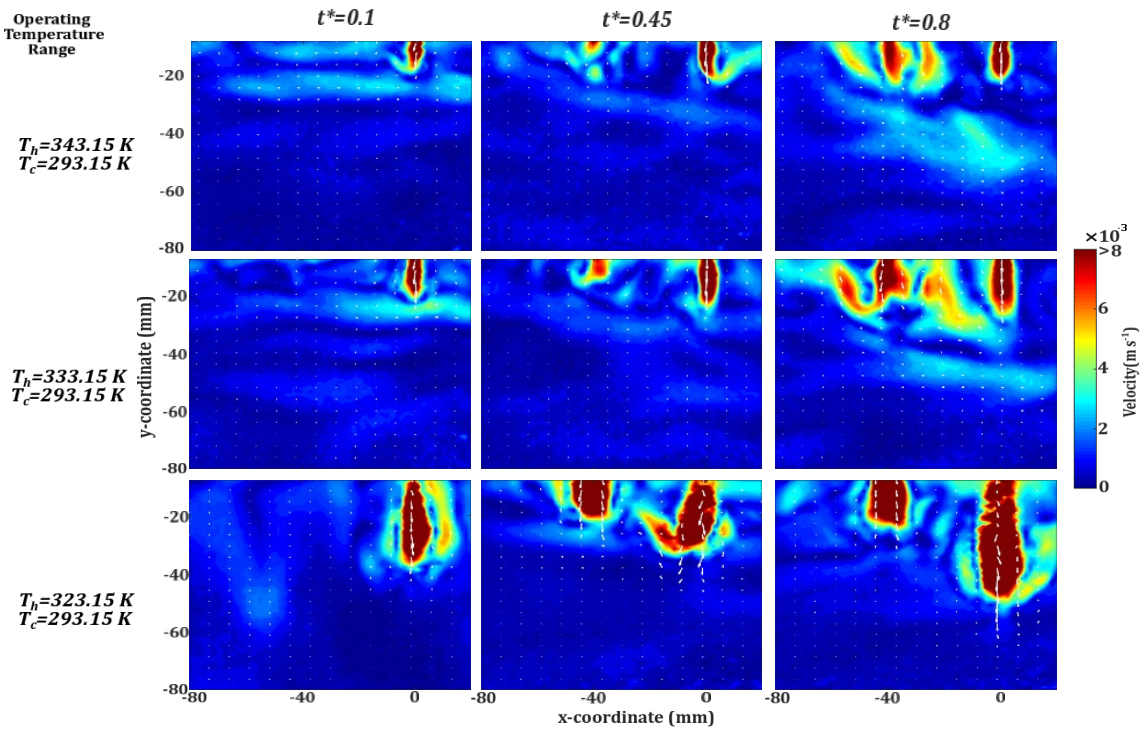

Fig. 16. Velocity profiles for different working temperature differences at t^*=0.1, t^*=0.45 and t^*=0.8 with optimized orifice baffle. Condition: Q_{in} = 1 L min^{-1}.

Unlike the fluid structure of the initial uniform OBD case, only a tiny jet through the central orifice can be detected at $t^* = 0.1$ on Fig. 16. The front of thermal jet penetrates deeper with the decreasing ΔT value, due to reasons explained above. When the charging proceeds (e.g., $t^* = 0.45$), a second small jet appears at the location of the side orifice (the orifice at right side of the central orifice shown in Fig. 6a). The interaction between the adjacent entrained buoyant plumes then takes place, illustrated by the appearance of K–H instabilities or engulfment just below the upper baffle shown on Fig. 16. Nevertheless, this intense mixing region covers a very small depth. The temperature stratification could be well maintained, corroborated by the constant Ri_{bulk} values (Fig. 15a) that not decline until t^*>0.9. The thermo-hydrodynamic behaviors of the rising plumes generated by multiple (neighboring) thermal jets and their mutual interferences [59] are more complex and certainly deserve further systematic investigations, but are beyond the scope of this paper.

Note that these experiments were performed under Q_{in}=1 L·min^{-1}, for which the convective transport is the dominant heat transfer mechanism responsible for the thermocline decay. However, at low Q_{in} under which the real charging time is far prolonged, the influence of ΔT on the global thermal performance of the storage tank could be less significant because of the more important thermal diffusion and heat losses (as has been discussed in section 4.1). Under certain circumstances, an inverse trend might occur because smaller ΔT means smaller heat diffusion between the hot and cold fluids. Thinner thermocline zone could thereby be maintained over the long-time thermocline forwarding. More detailed discussion on this aspect has been provided in our earlier study [29]. Anyhow, the working ΔT should be carefully determined in connection with other influencing factors (i.e., Q_{in}; geometry of the storage tank; aimed application, etc.) to achieve a compromise between the convective and diffusive dominated heat transfers.

5. Conclusion and prospects

This article presents a numerical and experimental work on the characterization and management of the dynamic thermocline behaviors in a SMT storage tank. The first part of the study has been focused on the CFD simulation of the charging operation and on the optimization of the orifice configuration of the upper baffle using the algorithm proposed in our earlier study [43]. Conjugated fluid flow and heat transfer and complex thermo-hydrodynamic behaviors of the thermal jet were observed. In particular, the jet entrainment phenomenon featured by the rising buoyant plumes was shown to appear, which was provoked by the interactions between the inertia force of the inflowing jet and the buoyancy force due to the density (temperature) difference. Optimizing the size distribution of orifices on the upper baffle could effectively mitigate the impact of thermal jet on the temperature stratification, indicated by the increasing values of the $Ri_{gradient}$ number from one optimization step to the next (all higher than 1 at final step). In fact, the optimized OBD could prevent the thermal overturning, restrict the convection-dominated heat transfer (Pe_x<<1), and reach a balanced convection/diffusion transport along the *y*-direction(Pe_y=1) within a very small depth downstream the upper baffle, leading to more flattened and thinner thermocline compared to that of the initial uniform OBD case.

Charging experiments have then been performed for the lab-scale cuboid SMT storage tank equipped with initial uniform or optimized OBD. The evolution of the local velocity profiles under different injecting flow rates or temperatures were captured and recorded by the PIV method. The buoyant plumes and their dynamic evolution were clearly visualized. The results of PIV measurement and CFD simulation exhibit good agreement, indicating that the physical phenomenon of jet entrainment in SMT storage tank is well captured. The length of jet penetration for the initial uniform OBD was found to increase with the increasing inlet flowrate and the decreasing temperature difference, the weaker buoyancy force being more difficult to balance the momentum force. For the optimized OBD case, the impacts of both factors were found far less important due to the impeded central jet and by the plume interferences between the multiple jets. The global performances of the storage tank were also calculated and compared. A low Q_{in} and a large ΔT are positive factors to achieve a high storage capacity and charging efficiency if the inflowing momentum-dominated jet cannot be properly handled. But in real-world practice, the operating conditions should be well coordinated to guarantee a high energy efficiency. Results also shown that by using the optimized OBD the impacts of these operating factors are less significant and better thermal performances are achieved, , providing more rooms for selecting appropriate operating ranges of SMT storage systems in different aimed application fields.

As prospects, the synchronized measurement of velocity & temperature fields and their evolutions using appropriate optical-based method (e.g., LIF) is our goal. In this way, a thorough understanding of conjugated fluid flow and heat transfer characteristics may be acquired, necessary for developing some theoretical models to better predict the effect of thermal jet. Testing and comparing performances of different flow diffusers in a well-designed SMT storage tank under a wide range of operating conditions are an interesting direction for future work. Moreover, the extension of the (optimized) orifice distributor method to scaled-up SMT storage tanks applied to medium/high-temperature conditions is also the aim of future studies.

Acknowledgement

This work is supported by the French ANR within the project OPTICLINE (ANR-17-CE06–0013). Technical supports from Mr. Julien Aubril and Mr. Arnaud Arrivé at LTEN are gratefully acknowledged.

Appendix A: Further comparison between the PIV and CFD results on the velocity profiles

In Fig. 4, we compared the measured and simulated HTF velocity fields at three moments during the charging course. Here a more detailed comparison is given on the velocity magnitude and *x*, *y* components at different positions of the SMT tank. PIV and CFD results at three charging times (t^*) are displayed in Figs. A1-A3, showing generally good agreement.

At t^*=0.12 (Fig. A1), the v_y profile along *y*-direction shows that the inertia-forced thermal jet could be balanced out, and velocity profile goes slightly upward once it passes the neutral point. A difference on the penetration length (h_j) between the PIV and CFD results could be detected, as explained in Fig. 5 of the paper. The v_y profile along *x*-direction (e.g., y =-20 mm or -80 mm) shows that the measured buoyant plumes by PIV tend to expand and rise, leading to the flow recirculation especially in the lateral zones. As the charging time increases (Figs. A2-A3), the zones impacted by the thermal jet enlarges and the neutral point advances, due to the heated up fluid temperature along the central line (x=0) and the reduced buoyancy force. The necessity of the structured inlet flow diffusor is thereby highlighted so as to better mitigate the mixing effect of inflowing thermal jet.

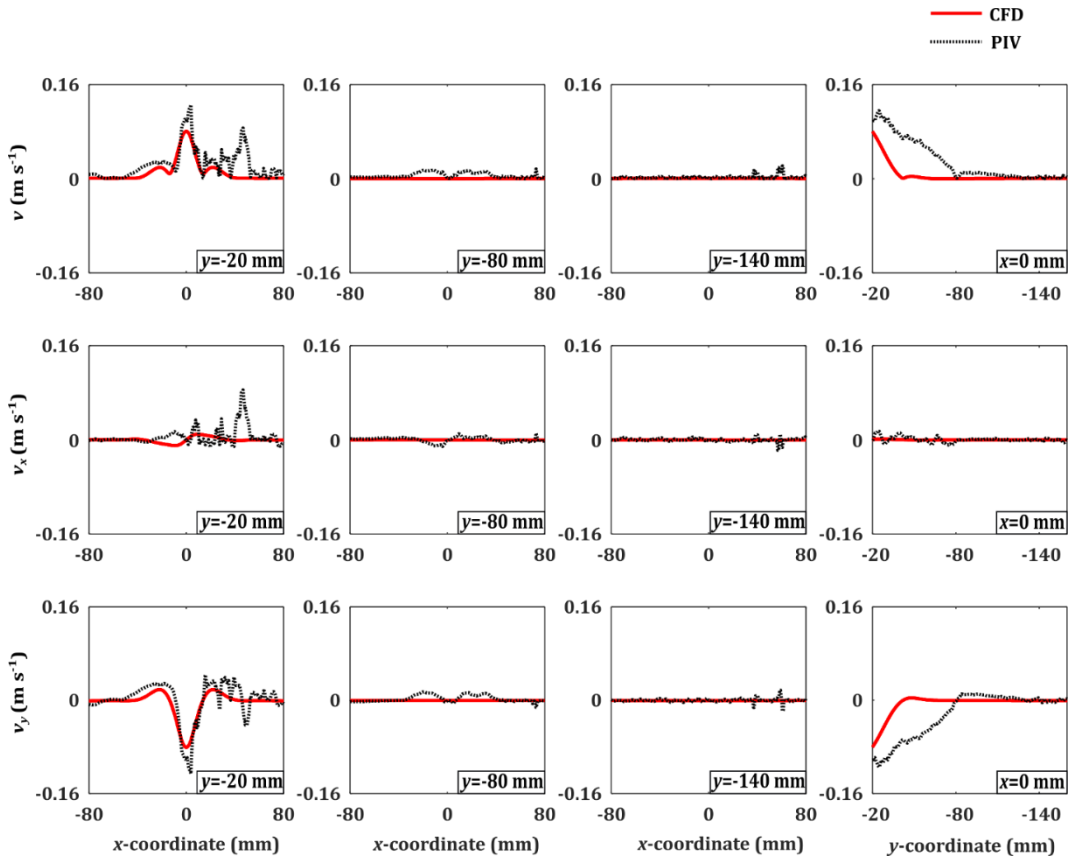

Fig. A1. Comparison of velocity profiles between CFD and PIV at t=100 s (t^*=0.12). Conditions: $Q_{in} = 1$ L min^{-1} with initial uniform OBD

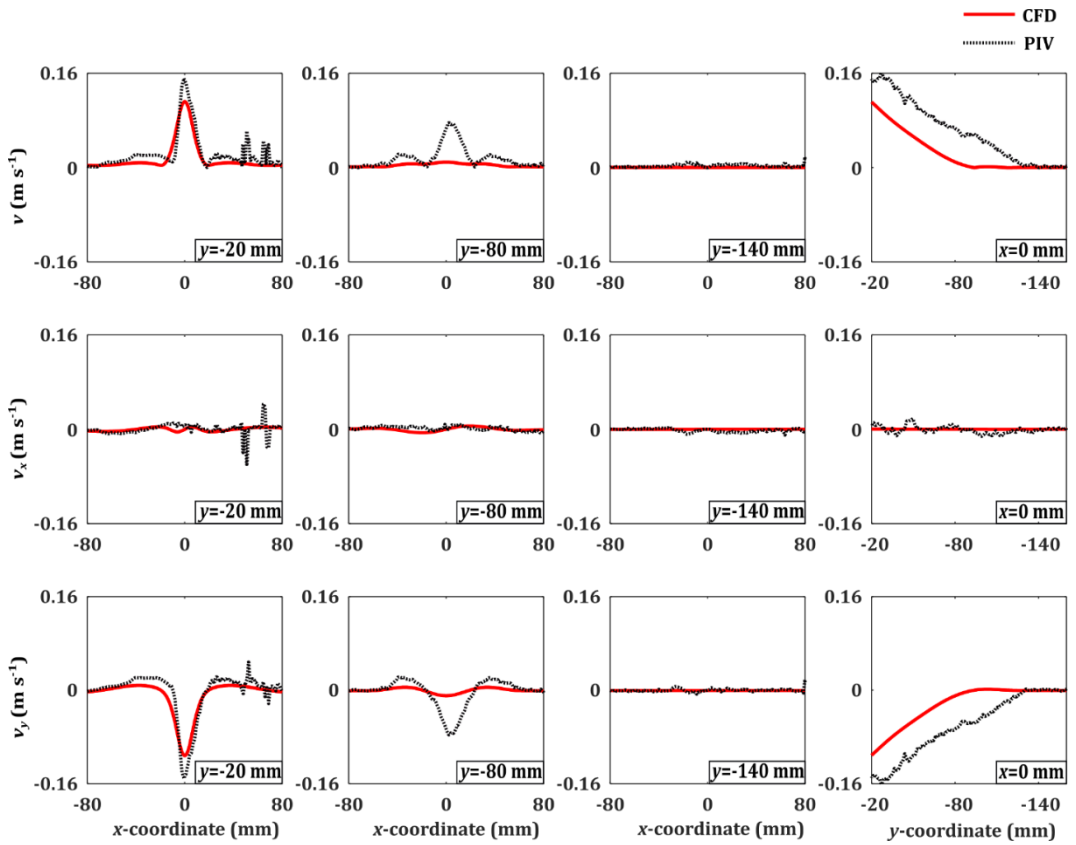

Fig. A2. Comparison of velocity profiles between CFD and PIV at t=400 s (t^*=0.47). Conditions: $Q_{in} = 1$ L min^{-1} with initial uniform OBD

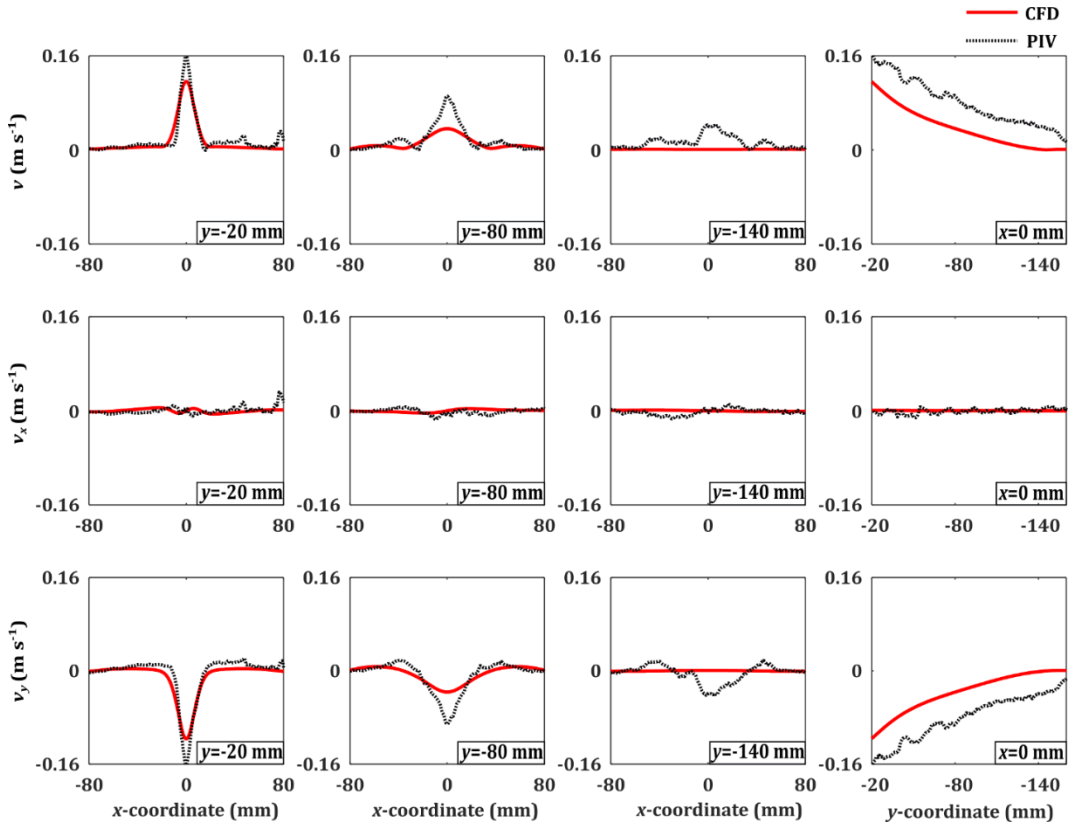

Fig. A3. Comparison of velocity profiles between CFD and PIV at t=700 s (t^*=0.82). Conditions: $Q_{in} = 1$ L min^{-1} with initial uniform OBD

References

[1] B. Xie, N. Baudin, J. Soto, Y. Fan, L. Luo, Thermocline packed bed thermal energy storage system, in: Renew. Energy Prod. Distrib., Elsevier, 2022: pp. 325–385. https://doi.org/10.1016/B978-0-323-91892-3.24001-6.

[2] I. Al Asmi, K. Knobloch, R. Le Goff Latimier, T. Esence, K. Engelbrecht, H. Ben Ahmed, Thermocline thermal storage modeling towards its predictive optimal management, J. Energy Storage. 52 (2022) 104979. https://doi.org/10.1016/j.est.2022.104979.

[3] A. Abánades, J. Rodríguez-Martín, J.J. Roncal, A. Caraballo, F. Galindo, Proposal of a thermocline molten salt storage tank for district heating and cooling, Appl. Therm. Eng. 218 (2023) 119309. https://doi.org/10.1016/j.applthermaleng.2022.119309.

[4] D. Le Roux, Y. Lalau, B. Rebouillat, P. Neveu, R. Olivès, Thermocline thermal energy storage optimisation combining exergy and life cycle assessment, Energy Convers. Manag. 248 (2021) 114787. https://doi.org/10.1016/j.enconman.2021.114787.

[5] D. Le Roux, R. Olivès, P. Neveu, Geometry optimisation of an industrial thermocline Thermal Energy Storage combining exergy, Life Cycle Assessment and Life Cycle Cost Analysis, J. Energy Storage. 55 (2022) 105776. https://doi.org/10.1016/j.est.2022.105776.

[6] Els.S. ELSihy, C. Xu, X. Du, Cyclic performance of cascaded latent heat thermocline energy storage systems for high-temperature applications, Energy. 239 (2022) 122229. https://doi.org/10.1016/j.energy.2021.122229.

[7] S. Advaith, D.R. Parida, K.T. Aswathi, N. Dani, U.K. Chetia, K. Chattopadhyay, S. Basu, Experimental investigation on single-medium stratified thermal energy storage system, Renew. Energy. 164 (2021) 146–155. https://doi.org/10.1016/j.renene.2020.09.092.

[8] D.H. Kim, S.H. Yoon, Y. Kim, K.H. Lee, J.S. Choi, Experimental studies on the charging performance of single-tank single-medium thermal energy storage, Appl. Therm. Eng. 149 (2019) 1098–1104. https://doi.org/10.1016/j.applthermaleng.2018.12.062.

[9] S. Vannerem, P. Neveu, Q. Falcoz, Experimental investigation of the impact of fluid distribution on thermocline storage performance, J. Energy Storage. 52 (2022) 104864. https://doi.org/10.1016/j.est.2022.104864.

[10] L. Milton-McGurk, N. Williamson, S.W. Armfield, M.P. Kirkpatrick, Characterising entrainment in fountains and negatively buoyant jets, J. Fluid Mech. 939 (2022) A29. https://doi.org/10.1017/jfm.2022.152.

[11] K.G.T. Hollands, M.F. Lightstone, A review of low-flow, stratified-tank solar water heating systems, Sol. Energy. 43 (1989) 97–105. https://doi.org/10.1016/0038-092X(89)90151-5.

[12] D. Yang, B. Chen, S.A. Socolofsky, M. Chamecki, C. Meneveau, Large-eddy simulation and parameterization of buoyant plume dynamics in stratified flow, J. Fluid Mech. 794 (2016) 798–833. https://doi.org/10.1017/jfm.2016.191.

[13] L.-A. Couston, D. Lecoanet, B. Favier, M. Le Bars, Dynamics of mixed convective–stably-stratified fluids, Phys. Rev. Fluids. 2 (2017) 094804. https://doi.org/10.1103/PhysRevFluids.2.094804.

[14] J. Rendall, A. Abu-Heiba, K. Gluesenkamp, K. Nawaz, W. Worek, A. Elatar, Nondimensional convection numbers modeling thermally stratified storage tanks: Richardson's number and hot-water tanks, Renew. Sustain. Energy Rev. 150 (2021) 111471. https://doi.org/10.1016/j.rser.2021.111471.

[15] A. Zachár, Analytic solution for convection dominant heat transport induced by buoyant jet entrainment inside hot fluid storage tanks, Sol. Energy. 195 (2020) 239–248. https://doi.org/10.1016/j.solener.2019.11.008.

[16] W.R. Peltier, C.P. Caulfield, M <scp>IXING</scp> E <scp>FFICIENCY IN</scp> S <scp>TRATIFIED</scp> S <scp>HEAR</scp> F <scp>LOWS</scp>, Annu. Rev. Fluid Mech. 35 (2003) 135–167. https://doi.org/10.1146/annurev.fluid.35.101101.161144.

[17] M.Y. Haller, C.A. Cruickshank, W. Streicher, S.J. Harrison, E. Andersen, S. Furbo, Methods to determine stratification efficiency of thermal energy storage processes – Review and theoretical comparison, Sol. Energy. 83 (2009) 1847–1860. https://doi.org/10.1016/j.solener.2009.06.019.

[18] Q. Li, X. Huang, Y. Tai, W. Gao, L. Wenxian, W. Liu, Thermal stratification in a solar hot water storage tank with mantle heat exchanger, Renew. Energy. 173 (2021) 1–11. https://doi.org/10.1016/j.renene.2021.03.105.

[19] S. Hatte, C. Mira-Hernández, S. Advaith, A. Tinaikar, U.K. Chetia, K.V. Manu, K. Chattopadhyay, J.A. Weibel, S. V. Garimella, V. Srinivasan, S. Basu, Short and long-term sensitivity of lab-scale thermocline based thermal storage to flow disturbances, Appl. Therm. Eng. 109 (2016) 936–948. https://doi.org/10.1016/j.applthermaleng.2016.04.138.

[20] V. Joshi, C. Wasnik, A. Wadegaonkar, S.B. Kedare, M. Bose, Influence of porosity and permeability of flow distributor on thermal stratification in single media storage tank, J. Energy Storage. 44 (2021) 103241. https://doi.org/10.1016/j.est.2021.103241.

[21] A.A. Dehghan, A. Barzegar, Thermal performance behavior of a domestic hot water solar storage tank during consumption operation, Energy Convers. Manag. 52 (2011) 468–476.

https://doi.org/10.1016/j.enconman.2010.06.075.

[22] D.J. Nizami, M.F. Lightstone, S.J. Harrison, C.A. Cruickshank, Negative buoyant plume model for solar domestic hot water tank systems incorporating a vertical inlet, Sol. Energy. 87 (2013) 53–63. https://doi.org/10.1016/j.solener.2012.10.001.

[23] R. De Césaro Oliveski, A. Krenzinger, H.A. Vielmo, Comparison between models for the simulation of hot water storage tanks, Sol. Energy. 75 (2003) 121–134. https://doi.org/10.1016/j.solener.2003.07.009.

[24] Y. Bai, Z. Wang, J. Fan, M. Yang, X. Li, L. Chen, G. Yuan, J. Yang, Numerical and experimental study of an underground water pit for seasonal heat storage, Renew. Energy. 150 (2020) 487–508. https://doi.org/10.1016/j.renene.2019.12.080.

[25] C. Mira-Hernández, S.M. Flueckiger, S.V. Garimella, Numerical Simulation of Single- and Dual-media Thermocline Tanks for Energy Storage in Concentrating Solar Power Plants, Energy Procedia. 49 (2014) 916–926. https://doi.org/10.1016/j.egypro.2014.03.099.

[26] J. Dragsted, S. Furbo, M. Dannemand, F. Bava, Thermal stratification built up in hot water tank with different inlet stratifiers, Sol. Energy. 147 (2017) 414–425. https://doi.org/10.1016/j.solener.2017.03.008.

[27] Y.P. Chandra, T. Matuska, Numerical prediction of the stratification performance in domestic hot water storage tanks, Renew. Energy. 154 (2020) 1165–1179. https://doi.org/10.1016/j.renene.2020.03.090.

[28] M. Pilotelli, B. Grassi, A.M. Lezzi, G.P. Beretta, Flow models of perforated manifolds and plates for the design of a large thermal storage tank for district heating with minimal maldistribution and thermocline growth, Appl. Energy. 322 (2022) 119436. https://doi.org/10.1016/j.apenergy.2022.119436.

[29] W. Lou, B. Xie, J. Aubril, Y. Fan, L. Luo, A. Arrivé, Optimized flow distributor for stabilized thermal stratification in a single-medium thermocline storage tank: A numerical and experimental study, Energy. 263 (2023) 125709. https://doi.org/10.1016/j.energy.2022.125709.

[30] L. Kocijel, V. Mrzljak, V. Glažar, Pressure drop in large volumetric heat storage tank radial plate diffuser, J. Energy Storage. 29 (2020) 101350. https://doi.org/10.1016/j.est.2020.101350.

[31] J. Weiss, I. Ortega-Fernández, R. Müller, D. Bielsa, T. Fluri, Improved thermocline initialization through optimized inlet design for single-tank thermal energy storage systems, J. Energy Storage. 42 (2021) 103088. https://doi.org/10.1016/j.est.2021.103088.

[32] D.R. Parida, S. Advaith, N. Dani, S. Basu, Assessing the impact of a novel hemispherical diffuser on a single-tank sensible thermal energy storage system, Renew. Energy. 183 (2022) 202–218. https://doi.org/10.1016/j.renene.2021.10.099.

[33] Q. Li, W. Lin, X. Huang, Y. Tai, X. Ding, Y. Zhang, W. Gao, Thermocline dynamics in a thermally stratified water tank under different operation modes, Appl. Therm. Eng. 212 (2022) 118560. https://doi.org/10.1016/j.applthermaleng.2022.118560.

[34] W. Lou, L. Luo, Y. Hua, Y. Fan, Z. Du, A Review on the Performance Indicators and Influencing Factors for the Thermocline Thermal Energy Storage Systems, Energies. 14 (2021) 8384. https://doi.org/10.3390/en14248384.

[35] M. Gasque, F. Ibáñez, P. González-Altozano, Minimum Number of Experimental Data for the Thermal Characterization of a Hot Water Storage Tank, Energies. 14 (2021) 4741. https://doi.org/10.3390/en14164741.

[36] J. van Berkel, C.C.M. Rindt, A.A. van Steenhoven, Thermocline dynamics in a thermally stratified store, Int. J. Heat Mass Transf. 45 (2002) 343–356. https://doi.org/10.1016/S0017-9310(01)00161-2.

[37] L.J. Shah, E. Andersen, S. Furbo, Theoretical and experimental investigations of inlet stratifiers for solar storage tanks, Appl. Therm. Eng. 25 (2005) 2086–2099. https://doi.org/10.1016/j.applthermaleng.2005.01.011.

[38] E. Andersen, S. Furbo, M. Hampel, W. Heidemann, H. Müller-Steinhagen, Investigations on stratification devices for hot water heat stores, Int. J. Energy Res. 32 (2008) 255–263. https://doi.org/10.1002/er.1345.

[39] A. Tinaikar, S. Advaith, U.K. Chetia, K.V. Manu, S. Basu, Spatio-temporal disruption of thermocline by successive laminar vortex pairs in a single tank thermal energy storage, Appl. Therm. Eng. 109 (2016) 924–935. https://doi.org/10.1016/j.applthermaleng.2016.04.105.

[40] S. Wang, J.H. Davidson, Performance of a rigid porous-tube stratification manifold in comparison to an inlet pipe, Sol. Energy. 146 (2017) 298–308. https://doi.org/10.1016/j.solener.2017.02.045.

[41] A. Al-Habaibeh, B. Shakmak, S. Fanshawe, Assessment of a novel technology for a stratified hot water energy storage – The water snake, Appl. Energy. 222 (2018) 189–198. https://doi.org/10.1016/j.apenergy.2018.04.014.

[42] P. Gajbhiye, S. Kedare, M. Bose, Experimental analysis of parameters influencing thermal stratification in single media single tank storage system with flow distributor, Therm. Sci. Eng. Prog. 30 (2022) 101243. https://doi.org/10.1016/j.tsep.2022.101243.

[43] W. Lou, Y. Fan, L. Luo, Single-tank thermal energy storage systems for concentrated solar power: Flow distribution

optimization for thermocline evolution management, J. Energy Storage. 32 (2020) 101749. https://doi.org/10.1016/j.est.2020.101749.

[44] Z. Wang, H. Zhang, B. Dou, H. Huang, W. Wu, Z. Wang, Experimental and numerical research of thermal stratification with a novel inlet in a dynamic hot water storage tank, Renew. Energy. 111 (2017) 353–371. https://doi.org/10.1016/j.renene.2017.04.007.

[45] W. Bahnfleth, J. Song, J. Cimbala, Measured and Modeled Charging of a Stratified Chilled Water Thermal Storage Tank with Slotted Pipe Diffusers, HVAC&R Res. 9 (2003) 467–491. https://doi.org/10.1080/10789669.2003.10391081.

[46] A. Li, F. Cao, W. Zhang, B. Shi, H. Li, Effects of different thermal storage tank structures on temperature stratification and thermal efficiency during charging, Sol. Energy. 173 (2018) 882–892. https://doi.org/10.1016/j.solener.2018.08.025.

[47] Z.Y. Li, W.Q. Tao, A New Stability-Guaranteed Second-Order Difference Scheme, Numer. Heat Transf. Part B Fundam. 42 (2002) 349–365. https://doi.org/10.1080/10407790190053987.

[48] R. Bayón, E. Rojas, Simulation of thermocline storage for solar thermal power plants: From dimensionless results to prototypes and real-size tanks, Int. J. Heat Mass Transf. 60 (2013) 713–721. https://doi.org/10.1016/j.ijheatmasstransfer.2013.01.047.

[49] R. Majumdar, S.K. Saha, Effect of varying extent of PCM capsule filling on thermal stratification performance of a storage tank, Energy. 178 (2019) 1–20. https://doi.org/10.1016/j.energy.2019.04.101.

[50] H.D.I. Abarbanel, D.D. Holm, J.E. Marsden, T. Ratiu, Richardson Number Criterion for the Nonlinear Stability of Three-Dimensional Stratified Flow, Phys. Rev. Lett. 52 (1984) 2352–2355. https://doi.org/10.1103/PhysRevLett.52.2352.

[51] D. Li, A. Anis, F. Al Senafi, Neap-spring variability of tidal dynamics in the Northern Arabian Gulf, Cont. Shelf Res. 197 (2020) 104086. https://doi.org/10.1016/j.csr.2020.104086.

[52] V. Panthalookaran, M.F. El-Amin, W. Heidemann, H. Müller-Steinhagen, Calibrated models for simulation of stratified hot water heat stores, Int. J. Energy Res. 32 (2008) 661–676. https://doi.org/10.1002/er.1423.

[53] R.J. Moffat, Describing the uncertainties in experimental results, Exp. Therm. Fluid Sci. 1 (1988) 3–17. https://doi.org/10.1016/0894-1777(88)90043-X.

[54] B. Xie, N. Baudin, J. Soto, Y. Fan, L. Luo, Experimental and numerical study on the thermocline behavior of packed-bed storage tank with sensible fillers, Renew. Energy. 209 (2023) 106–121. https://doi.org/10.1016/j.renene.2023.03.107.

[55] W. Yaïci, M. Ghorab, E. Entchev, S. Hayden, Three-dimensional unsteady CFD simulations of a thermal storage tank performance for optimum design, Appl. Therm. Eng. 60 (2013) 152–163. https://doi.org/10.1016/j.applthermaleng.2013.07.001.

[56] Y.P. Chandra, T. Matuska, Stratification analysis of domestic hot water storage tanks: A comprehensive review, Energy Build. 187 (2019) 110–131. https://doi.org/10.1016/j.enbuild.2019.01.052.

[57] W. Shaikh, A. Wadegaonkar, S.B. Kedare, M. Bose, Numerical simulation of single media thermocline based storage system, Sol. Energy. 174 (2018) 207–217. https://doi.org/10.1016/j.solener.2018.08.084.

[58] G. Wang, S. Yu, S. Niu, Z. Chen, P. Hu, A comprehensive parametric study on integrated thermal and mechanical performances of molten-salt-based thermocline tank, Appl. Therm. Eng. 170 (2020) 115010. https://doi.org/10.1016/j.applthermaleng.2020.115010.

[59] A.C.H. Lai, J.H.W. Lee, Dynamic interaction of multiple buoyant jets, J. Fluid Mech. 708 (2012) 539–575. https://doi.org/10.1017/jfm.2012.332.